A General Acceleration Method for the Analysis of Frequency Selective Surfaces

BY

S.W. RIENSTRA

EINDHOVEN UNIVERSITY OF TECHNOLOGY

JANUARY 2002

under contract no. WDC262A “Frequency Selective Surfaces” between Thales Naval Nederland and the departments of Electrical Engineering and Mathematics and Computer Science of the Eindhoven University of Technology.

January 22, 2002

Contents

Contents 0

1 Summary 1

2 Introduction 1

3 The general problem 2

4 Accelerating the series 7

5 Evaluation of the asymptotic series $\zeta_{nn'}^{(j)}$ 8

6 A transformation for small ρ using Poisson's formula 9

6.1 Poisson's Formula 9
6.2 An exponential regularisation 10
6.3 The final result 11

7 Rooftop basis functions 12

7.1 Analysis 12
7.2 Auxiliary functions 13
7.3 Tables 15

8 The strip 16

8.1 The orthogonal array 17

9 The gridded square 18

10 The single homogeneous layer 19

10.1 Reflection and transmission coefficients 19
10.2 Asymptotic expansions for large k 20

11 Examples 21

12 Conclusions 24

Implementation 24

Brief summary of the method 25

Acknowledgements 25

References 26

13 Figures of examples 27

1 Summary

A general theory is presented to accelerate slowly converging series, that occur in the numerical solution of the electromagnetic scattering problem of Frequency Selective Surfaces. It consists of three steps. (1) A Kummer transformation-type step, where the asymptotically slow part of the series ($O(1/k)$, $O(1/k^3)$, etc.) is subtracted, and taken apart. (2) An Ewald transformation-type step, where the algebraically slow converging parts $O(1/k^n)$ are turned into exponentially convergent integrals of the type $\sim \mathrm{e}^{-k^2\rho^2}$. (3) A Poisson transformation step, in order to transform the relatively slow convergence $\sim \mathrm{e}^{-k^2\rho^2}$ for small ρ into a fast convergence $\sim \mathrm{e}^{-k^2/\rho^2}$.

The technique presented is very general. However, the necessary Fourier transforms are in general probably to be evaluated numerically, as they are only explicitly available for sufficiently simple basis and test functions.

Examples of such explicit forms (rooftop basis functions applied to geometries with a single strip, single square, gridded square) are included.

2 Introduction

Thales Naval Nederland (Common Technical Business Unit Front End) and the *Eindhoven University of Technology* (the departments of Electrical Engineering and Mathematics and Computer Science) have commenced a project on fundamental research on Frequency Selective Surfaces (FSS). These are arrays of metallic patches on thin dielectric substrates, or a conducting sheet periodically perforated with apertures. They behave as filters. Incident electromagnetic waves are reflected at some frequencies but are transmitted through the surface at others. They can be incorporated in microwave reflector antennas to enable the system to operate over two or more frequency ranges simultaneously.

The research involves analysis of the interaction of the arrays with electromagnetic waves so that CAD software can be developed. The usual method of simple equivalent circuits to model the arrays and predict the transmission response is not followed. Here the more powerful technique of modal analysis is developed to predict the complete performance including polarization effect.

In order to make progress, the array is modelled as infinitely periodic. In this way the resulting integral equation over the surface can be reduced to an equation over one cell, while the kernel (resulting from the Green's function) is described by infinite series.

The integral equation is numerically solved by rewriting the integral into a matrix equation. After having reduced the problem to this form, the resulting problem is to evaluate the matrix elements.

These matrix elements consist of the same infinite series as the integral kernel, but now multiplied by the basis and test functions used for the numerical solution.

It appears that the infinite series converges notoriously slowly. Details depend on the smoothness of the basis functions used, but typically it is only algebraically in k^{-2}, if $\boldsymbol{k}$ is (proportional to) the 2D series index vector. Furthermore, it appears that smooth basis functions are **not** to be recommended because of a much poorer behaviour to the

numerical solution of the integral equation. Therefore, the selected basis functions, preferred for good numerical results, produce convergence of only $O(1/k^2)$.

The aim of the present report is to present a general acceleration technique in order to render the series highly convergent.

3 The general problem

We are interested in the matrix equation

$$\mathcal{Z}\mathcal{I} = \mathcal{V} \qquad \text{or} \qquad \sum_{n'=1}^{N} Z_{nn'} I_{n'} = V_n \quad \text{where } n = 1 \ldots N, \tag{1}$$

which is a numerical representation of the FSS-scattering integral equation, given by Tijhuis [1, 2].

In an (x, y, z)-cartesian coordinate system where $\boldsymbol{r} = x\boldsymbol{u}_x + y\boldsymbol{u}_y + z\boldsymbol{u}_z$ with unit vectors $\boldsymbol{u}_x, \boldsymbol{u}_y, \boldsymbol{u}_z$, the surface of interest is the (x, y)-plane given by $z = 0$. The component of a vector $\boldsymbol{r} = (x, y, z)$ that lies in the surface is given by

$$\boldsymbol{r}_T = (x, y, 0) = (\boldsymbol{u}_z \times \boldsymbol{r}) \times \boldsymbol{u}_z.$$

The FSS-scattering integral determines the electric current $\boldsymbol{J}_S^e(\boldsymbol{r}_T)$, in $z = 0$, on the elementary cell S_{oo} spanned by the vectors $\boldsymbol{a}_1$ and $\boldsymbol{a}_2$.

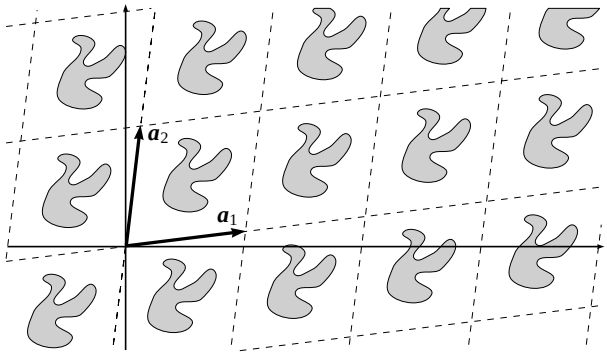

Figure 1: Sketch of geometry of array of metallized patches.

The current is the result of the scattered incident plane wave (incident from below, $z < 0$) with electric field strength $\boldsymbol{E}^i(\boldsymbol{r}) = \boldsymbol{u}^p \exp(\mathrm{i}\boldsymbol{k}^i \cdot \boldsymbol{r})$, where $\boldsymbol{k}^i = \boldsymbol{u}^i k_0$, and $k_0 = \omega/c_0$ is the free field wave number at circular frequency ω and light speed c_0. The corresponding magnetic field strength is $\boldsymbol{H}^i(\boldsymbol{r}) = Y_0 \boldsymbol{u}^i \times \boldsymbol{u}^p \exp(\mathrm{i}\boldsymbol{k}^i \cdot \boldsymbol{r})$, where $Y_0^{-1} = Z_0 = \sqrt{\mu_0/\varepsilon_0}$ is the free space wave impedance with permittivity ε_0 and permeability μ_0. Note that $c_0^2 = 1/\varepsilon_0\mu_0$.

$\boldsymbol{u}^p$ is the direction of E-polarization, and $\boldsymbol{u}^i$ the direction of incidence. As the polarization of a plane wave is always perpendicular to the direction of propagation (it is a transverse wave), we have $\boldsymbol{u}^p \cdot \boldsymbol{u}^i = 0$. If φ^i denotes the angle in the (x, y)-plane and θ^i denotes the angle with the z-axis, we can write

$$\boldsymbol{u}^i = \sin\theta^i \cos\varphi^i \boldsymbol{u}_x + \sin\theta^i \sin\varphi^i \boldsymbol{u}_y + \cos\theta^i \boldsymbol{u}_z,$$

and similar for $\boldsymbol{u}^p$, where orthogonality of $\boldsymbol{u}^i$ and $\boldsymbol{u}^p$ is guaranteed if

$$\sin\theta^i \sin\theta^p \cos(\varphi^i - \varphi^p) + \cos\theta^i \cos\theta^p = 0.$$

The solution vector $\mathcal{I} = (I_n)$ of (1) determines a numerical representation of electric current $\boldsymbol{J}_S^e(\boldsymbol{r}_T)$ by the assumed expansion

$$\boldsymbol{J}_S^e(\boldsymbol{r}_T) \simeq \sum_{n=1}^{N} I_n \boldsymbol{J}_n(\boldsymbol{r}_T), \tag{2}$$

where I_n are scalar coefficients, and $\boldsymbol{J}_n$ are vectorial expansion functions, defined, together with their corresponding test functions $\boldsymbol{K}_n$, on the surface $z = 0$ with support $S_n \subset S_\infty$.

The right-hand side of equation (1) is given from the plane wave field $\boldsymbol{E}_T^{pl}$ that would result from the incident wave in the absence of metallization

$$\begin{aligned}\boldsymbol{E}_T^{pl}(\boldsymbol{r}_T) &= \Big\{\boldsymbol{u}_T^i\big(\boldsymbol{u}_T^i \cdot \boldsymbol{u}^p\big)\big(1 - R^e(k_T^i)\big) + \\ &\qquad \big(\boldsymbol{u}_z \times \boldsymbol{u}_T^i\big)\big(\boldsymbol{u}_z \times \boldsymbol{u}_T^i \cdot \boldsymbol{u}^p\big)\big(1 + R^h(k_T^i)\big)\Big\} \exp(\mathrm{i}\boldsymbol{k}_T^i \cdot \boldsymbol{r}_T) \\ &= \hat{\boldsymbol{E}}_T^{pl} \exp(\mathrm{i}\boldsymbol{k}_T^i \cdot \boldsymbol{r}_T)\end{aligned} \tag{3}$$

where $\boldsymbol{u}_T^i = \boldsymbol{k}_T^i / k_T^i$ and R^e and R^h are coefficients coresponding to reflection without metallization, as follows:

$$V_n = -\iint_{S_n} \boldsymbol{K}_n(\boldsymbol{r}_T) \cdot \boldsymbol{E}_T^{pl}(\boldsymbol{r}_T)\, \mathrm{d}A. \tag{4}$$

$\boldsymbol{E}_T^{pl}$ is the (x, y)-plane component of $\boldsymbol{E}^{pl}$.

The $N \times N$ matrix $\mathcal{Z}$ has the following matrix elements

$$Z_{nn'} = -Z_{nn'}^{(1)} + Z_{nn'}^{(2)}, \tag{5}$$

where $n, n' = 1 \cdots N$, and

$$Z_{nn'}^{(1)} = \frac{1}{4\pi^2} \iint_{-\infty}^{\infty} \hat{\alpha}_{nn'}^{(1)}(\boldsymbol{k}) \hat{G}_1(\boldsymbol{k})\, \mathrm{d}k_x \mathrm{d}k_y, \tag{6a}$$

$$Z_{nn'}^{(2)} = \frac{1}{4\pi^2} \iint_{-\infty}^{\infty} \hat{\alpha}_{nn'}^{(2)}(\boldsymbol{k}) \hat{G}_2(\boldsymbol{k})\, \mathrm{d}k_x \mathrm{d}k_y, \tag{6b}$$

and we defined with the Fourier transformed basis functions $\boldsymbol{J}_n$ and test functions $\boldsymbol{K}_n$

$$\hat{\alpha}_{nn'}^{(1)}(\boldsymbol{k}) = \big[-\mathrm{i}\boldsymbol{k} \cdot \hat{\boldsymbol{K}}_n^*(\boldsymbol{k})\big]\big[\mathrm{i}\boldsymbol{k} \cdot \hat{\boldsymbol{J}}_{n'}(\boldsymbol{k})\big], \tag{7a}$$

$$\hat{\alpha}_{nn'}^{(2)}(\boldsymbol{k}) = \big[\hat{\boldsymbol{K}}_n^*(\boldsymbol{k}) \cdot \hat{\boldsymbol{J}}_{n'}(\boldsymbol{k})\big]. \tag{7b}$$

The superscript "*" denotes a complex conjugate, and the spatial Fourier transform and its inverse of a function f are defined as

$$\hat{f}(\boldsymbol{k}) = \iint_{-\infty}^{\infty} f(\boldsymbol{x})\, \mathrm{e}^{-\mathrm{i}\boldsymbol{k}\cdot\boldsymbol{x}}\, \mathrm{d}\boldsymbol{x}, \quad f(\boldsymbol{x}) = \frac{1}{4\pi^2} \iint_{-\infty}^{\infty} \hat{f}(\boldsymbol{k})\, \mathrm{e}^{\mathrm{i}\boldsymbol{k}\cdot\boldsymbol{x}}\, \mathrm{d}\boldsymbol{k}. \tag{8}$$

For the following it is important to note that $\hat{\boldsymbol{K}}_n^*(\boldsymbol{k})$ is the Fourier transform of $\boldsymbol{K}_n(-\boldsymbol{x})$ and $-\mathrm{i}\boldsymbol{k}\cdot\hat{\boldsymbol{K}}_n^*(\boldsymbol{k})$ is the Fourier transform of $\nabla\cdot\boldsymbol{K}_n(-\boldsymbol{x})$, so by applying the convolution theorem (38), we have for $\alpha_{nn'}^{(j)}$

$$\alpha_{nn'}^{(1)}(\boldsymbol{x}) = \iint_{-\infty}^{\infty} \nabla\cdot\boldsymbol{K}_n(\boldsymbol{y})\,\nabla\cdot\boldsymbol{J}_{n'}(\boldsymbol{x}+\boldsymbol{y})\,\mathrm{d}\boldsymbol{y}, \tag{9a}$$

$$\alpha_{nn'}^{(2)}(\boldsymbol{x}) = \iint_{-\infty}^{\infty} \boldsymbol{K}_n(\boldsymbol{y})\cdot\boldsymbol{J}_{n'}(\boldsymbol{x}+\boldsymbol{y})\,\mathrm{d}\boldsymbol{y}. \tag{9b}$$

As the basis and test functions are chosen with compact support, also $\alpha_{nn'}^{(j)}(\boldsymbol{x})$ has a (slightly larger) compact support.

Note that

$$V_n = -\hat{\boldsymbol{E}}_T^{pl}\cdot\hat{\boldsymbol{K}}_n(-\boldsymbol{k}_T^i). \tag{10}$$

The Green's functions G_1 and G_2 are defined by

$$\hat{G}_j(\boldsymbol{k}) = \frac{4\pi^2 g_j(k)}{\boldsymbol{a}_1\cdot(\boldsymbol{a}_2\times\boldsymbol{u}_z)} \sum_{m_1=-\infty}^{\infty}\sum_{m_2=-\infty}^{\infty} \delta(\boldsymbol{k}-\boldsymbol{k}_T^i - m_1\boldsymbol{b}_1 - m_2\boldsymbol{b}_2), \tag{11}$$

$$g_1(k) = \frac{1}{k^2}\left(\frac{\gamma_1(k)}{\mathrm{i}\omega\varepsilon_0}\frac{R^e(k)-1}{2} + \frac{\mathrm{i}\omega\mu_0}{\gamma_1(k)}\frac{R^h(k)+1}{2}\right), \tag{12a}$$

$$g_2(k) = \frac{\mathrm{i}\omega\mu_0}{\gamma_1(k)}\frac{R^h(k)+1}{2}. \tag{12b}$$

$\boldsymbol{k}\equiv\boldsymbol{k}_T = k_x\boldsymbol{u}_x + k_y\boldsymbol{u}_y$ denotes the in-plane wave number, with modulus $k=|\boldsymbol{k}|$, and the complex square root γ_p is given by

$$\gamma_p(k) = \sqrt{k^2-\omega^2\varepsilon_p\mu_p}, \quad k=|\boldsymbol{k}| = \sqrt{k_x^2+k_y^2}, \tag{13}$$

with $p=1$ for the free field. Hence, $\varepsilon_1=\varepsilon_0$ and $\mu_1=\mu_0$. In general, the selected branch and branch cuts in the complex k-plane are important. As $\mathrm{e}^{-\mathrm{i}\omega t+\gamma_1 z}$ denotes a wave, outgoing to $z\to-\infty$, we need $\mathrm{Re}(\gamma_p)\geq 0$ for all $k\in\mathbb{C}$ with $\mathrm{Im}(\gamma_p)\leq 0$ if $\mathrm{Re}(\gamma_p)=0$. This corresponds to two L-shaped branch cuts, emanating from $k=k_p$ and $k=-k_p$ and touching each other at $k=0$. This is best portrayed in the following figure 2.

With the basis of the lattice given by $\boldsymbol{a}_1 = a_{1x}\boldsymbol{u}_x + a_{1y}\boldsymbol{u}_y$ and $\boldsymbol{a}_2 = a_{2x}\boldsymbol{u}_x + a_{2y}\boldsymbol{u}_y$, the basis of the reciprocal lattice is given by [1]

$$\begin{aligned}\boldsymbol{b}_1 &= 2\pi\frac{\boldsymbol{a}_2\times\boldsymbol{u}_z}{\boldsymbol{a}_1\cdot(\boldsymbol{a}_2\times\boldsymbol{u}_z)} = 2\pi\frac{a_{2y}\boldsymbol{u}_x - a_{2x}\boldsymbol{u}_y}{a_{1x}a_{2y}-a_{1y}a_{2x}},\\ \boldsymbol{b}_2 &= 2\pi\frac{\boldsymbol{u}_z\times\boldsymbol{a}_1}{\boldsymbol{a}_1\cdot(\boldsymbol{a}_2\times\boldsymbol{u}_z)} = 2\pi\frac{-a_{1y}\boldsymbol{u}_x + a_{1x}\boldsymbol{u}_y}{a_{1x}a_{2y}-a_{1y}a_{2x}}.\end{aligned} \tag{14}$$

Note that these are related by

$$\boldsymbol{A}^T\boldsymbol{B} = 2\pi \quad \text{if we define } \boldsymbol{A} = \begin{pmatrix} a_{1x} & a_{2x}\\ a_{1y} & a_{2y}\end{pmatrix}, \quad \boldsymbol{B} = \begin{pmatrix} b_{1x} & b_{2x}\\ b_{1y} & b_{2y}\end{pmatrix}, \tag{15}$$

[1] Note that $\boldsymbol{a}\cdot(\boldsymbol{b}\times\boldsymbol{c}) = \det(\boldsymbol{abc})$.

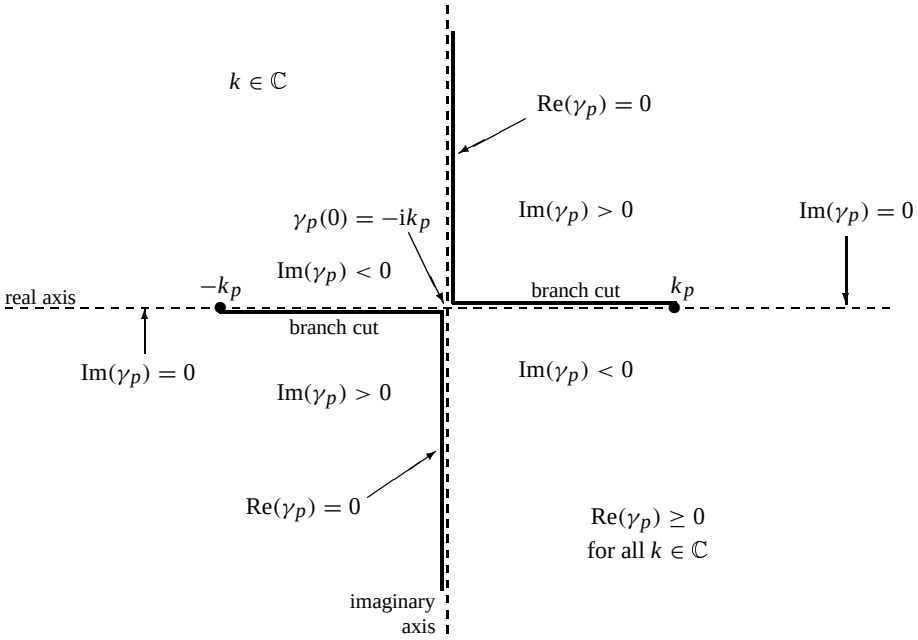

Figure 2: Details of branch cuts and signs of $\gamma_p(k) = \sqrt{k^2 - k_p^2}$ in the complex k-plane, where $k_p = \omega\sqrt{\varepsilon_p \mu_p}$ is real positive. The definition of $\gamma_p(k)$ adopted here is the branch of the multi-valued complex square root that corresponds to $\mathrm{Re}(\gamma_p) \geq 0$ for all k. $\mathrm{Re}(\gamma_p) = 0$ along the branch cuts. γ_p is positive real or negative imaginary along the real axis. Asymptotically, γ_p behaves like $\gamma_p(k) \simeq k\,\mathrm{sign}(\mathrm{Re}\,k)$ if $|k| \gg k_p$.

while $\det(\boldsymbol{A}) = \boldsymbol{a}_1 \cdot (\boldsymbol{a}_2 \times \boldsymbol{u}_z)$.

Utilizing the delta-functions in $\hat{G}_j$ we have finally

$$\det(\boldsymbol{A}) Z_{nn'}^{(j)} = \sum_{m_1=-\infty}^{\infty} \sum_{m_2=-\infty}^{\infty} \hat{\alpha}_{nn'}^{(j)}(\boldsymbol{k}) g_j(k), \tag{16}$$

where $\boldsymbol{k}$ now assumes specific values:

$$k_x = m_1 b_{1x} + m_2 b_{2x} + k_x^i, \quad k_y = m_1 b_{1y} + m_2 b_{2y} + k_y^i.$$

If we write $\boldsymbol{m} = m_1 \boldsymbol{u}_x + m_2 \boldsymbol{u}_y$, we have

$$\boldsymbol{k} = \boldsymbol{B}\boldsymbol{m} + \boldsymbol{k}_T^i, \quad \text{and} \quad \boldsymbol{m} = \tfrac{1}{2\pi} \boldsymbol{A}^T (\boldsymbol{k} - \boldsymbol{k}_T^i). \tag{17}$$

Further simplification is possible if the lattice is orthogonal. Without loss of generality we can assume that

$$\begin{gathered} \boldsymbol{a}_1 = a_1 \boldsymbol{u}_x, \;\; \boldsymbol{a}_2 = a_2 \boldsymbol{u}_y, \;\; \det(\boldsymbol{A}) = a_1 a_2, \\ \boldsymbol{b}_1 = b_1 \boldsymbol{u}_x, \;\; \boldsymbol{b}_2 = b_2 \boldsymbol{u}_y, \;\; b_1 = \tfrac{2\pi}{a_1}, \;\; b_2 = \tfrac{2\pi}{a_2}, \\ k_x = m_1 b_1 + k_x^i, \;\; k_y = m_2 b_2 + k_y^i. \end{gathered}$$

The power reflection coefficient

The reflected field (in $z < 0$) consists of an infinite sum of modes. Only the modes with a tangential phase speed larger than c_0, the speed of light, radiate un-attenuated into the far field, each in his own direction, given in the (x, y)-plane by the wave numbers

$$\boldsymbol{k}_{m_1m_2} = m_1\boldsymbol{b}_1 + m_2\boldsymbol{b}_2 + \boldsymbol{k}_T^i = k_0 \sin\theta_{m_1m_2}\big(\cos\varphi_{m_1m_2}\,\boldsymbol{u}_x + \sin\varphi_{m_1m_2}\,\boldsymbol{u}_y\big),$$

with corresponding z-component

$$-\mathrm{i}\gamma_1(k_{m_1m_2}) = -k_0\cos\theta_{m_1m_2}$$

for all m_1, m_2 within the Ewald circle, *i.e.* with $|\boldsymbol{k}_{m_1m_2}| < k_0$.

To quantify the effectiveness of the frequency selective surface one might compare the incident field with the reflected field. This is, however, not entirely straightforward as the reflected field radiates away into many directions. Therefore, Tijhuis [1] proposed a cell-averaged power reflection coefficient as follows.

The time-averaged incident power is given by

$$\langle \mathcal{P}_z^{\mathrm{in}} \rangle = \tfrac{1}{2} Y_0(\boldsymbol{u}^i \cdot \boldsymbol{u}_z). \tag{18}$$

$$\langle \mathcal{P}_z^{\mathrm{ref}} \rangle = \tfrac{1}{2} \sum_{\substack{\text{Ewald}\\ \text{circle}}} \Big(\frac{\omega\varepsilon_1}{k_1} \big| v^e_{m_1m_2} \big|^2 + \frac{k_1}{\omega\mu_1} \big| v^h_{m_1m_2} \big|^2 \Big) \tag{19}$$

where $\boldsymbol{k}_T = \boldsymbol{k}_{m_1m_2} = \boldsymbol{k}_T^i + m_1\boldsymbol{b}_1 + m_2\boldsymbol{b}_2$, $k_1 = |\gamma_1(k_T)|$, and

$$v^e_{m_1m_2} = \frac{\gamma_1}{\mathrm{i}\omega\varepsilon_0} \frac{1 - R^e(k_T)}{2} \Big(\frac{\mathrm{i}\boldsymbol{k}_T}{k_T} \cdot \frac{\hat{\boldsymbol{J}}_S^0(\boldsymbol{k}_T)}{\det(\boldsymbol{A})} \Big) \tag{20a}$$

$$v^h_{m_1m_2} = \frac{-\mathrm{i}\omega\mu_0}{\gamma_1} \frac{1 + R^h(k_T)}{2} \Big(\boldsymbol{u}_z \times \frac{\mathrm{i}\boldsymbol{k}_T}{k_T} \Big) \cdot \frac{\hat{\boldsymbol{J}}_S^0(\boldsymbol{k}_T)}{\det(\boldsymbol{A})}, \tag{20b}$$

while for $m_1 = m_2 = 0$ (when $\boldsymbol{k}_T = \boldsymbol{k}_T^i$) the part of the field that corresponds to a direct reflection at the dielectricum is to be added:

$$v^e_{0,0} = \frac{\mathrm{i}k_z^i}{k_T^i} \big(\boldsymbol{u}^p \cdot \boldsymbol{u}_z \big) R^e(k_T) + \frac{\gamma_1}{\mathrm{i}\omega\varepsilon_0} \frac{1 - R^e(k_T)}{2} \Big(\frac{\mathrm{i}\boldsymbol{k}_T}{k_T} \cdot \frac{\hat{\boldsymbol{J}}_S^0(\boldsymbol{k}_T)}{\det(\boldsymbol{A})} \Big) \tag{20c}$$

$$v^h_{0,0} = \frac{-\mathrm{i}k_0}{k_T^i} \big(\big(\boldsymbol{u}^i \times \boldsymbol{u}^p \big) \cdot \boldsymbol{u}_z \big) R^h(k_T) + \frac{-\mathrm{i}\omega\mu_0}{\gamma_1} \frac{1 + R^h(k_T)}{2} \Big(\boldsymbol{u}_z \times \frac{\mathrm{i}\boldsymbol{k}_T}{k_T} \Big) \cdot \frac{\hat{\boldsymbol{J}}_S^0(\boldsymbol{k}_T)}{\det(\boldsymbol{A})}. \tag{20d}$$

The reflection coefficient is then

$$\mathcal{R}_P = \frac{\langle \mathcal{P}_z^{\mathrm{ref}} \rangle}{\langle \mathcal{P}_z^{\mathrm{in}} \rangle}. \tag{21}$$

4 Accelerating the series

Unfortunately, the double series (16) appears to be slowly converging, and therefore as yet in this form of limited use in practice.

A first step to accelerate summation of the series is (a weaker form of) Kummer's transformation [6], which amounts to subtracting the asymptotic terms for large $|m_1|$ and large $|m_2|$. (Note that this corresponds with large k_x and large k_y.)

The rate of convergence is governed by the behaviour of $g_j(k)$ for large k. Since $g_j(k)$ ($j = 1, 2$) seems to behave asymptotically for large k like

$$g_j(k) = \frac{c_1^{(j)}}{k} + \frac{c_2^{(j)}}{k^3} + \ldots,$$

the typical leading order terms of the series (16) are of the following type

$$\left(\frac{c_1^{(j)}}{k} + \frac{c_2^{(j)}}{k^3} + \ldots\right) \hat{\alpha}_{nn'}^{(j)}(\boldsymbol{k}). \tag{22}$$

(For the demonstration, we will further restrict the asymptotic expansion to two terms. This is not at all essential, but it is probably sufficient for many applications.)

The essence of Kummer's transformation is that the asymptotic part is subtracted and added as follows

$$\boxed{\det(\boldsymbol{A}) Z_{nn'}^{(j)} = \sum_{m_1=-\infty}^{\infty} \sum_{m_2=-\infty}^{\infty} \left\{ \left(g_j(k) - \frac{c_1^{(j)}}{k} - \frac{c_2^{(j)}}{k^3} \right) \hat{\alpha}_{nn'}^{(j)}(\boldsymbol{k}) \right\} + \zeta_{nn'}^{(j)}} \tag{23}$$

where

$$\zeta_{nn'}^{(j)} = c_1^{(j)} \sum_{m_1=-\infty}^{\infty} \sum_{m_2=-\infty}^{\infty} \frac{\hat{\alpha}_{nn'}^{(j)}(\boldsymbol{k})}{k} + c_2^{(j)} \sum_{m_1=-\infty}^{\infty} \sum_{m_2=-\infty}^{\infty} \frac{\hat{\alpha}_{nn'}^{(j)}(\boldsymbol{k})}{k^3}, \tag{24}$$

and $\boldsymbol{k} = \boldsymbol{B}\boldsymbol{m} + \boldsymbol{k}_T^i$. Some care is to be taken if k vanishes for some m_1, m_2-combination.

Kummer's transformation gives instant results if the subtracted part is chosen such that it may be summed in closed form. This seems to be not the case here. However, we do have gained a lot, because

- the specific problem for given physical parameters and numerical method is reduced to the very general problem on the evaluation of

$$\sum_{m_1=-\infty}^{\infty} \sum_{m_2=-\infty}^{\infty} \frac{\hat{\alpha}_{nn'}^{(j)}(\boldsymbol{k})}{k^\ell}, \tag{25}$$

  related to the numerical method only;

- we use here only the asymptotic behaviour of $g_j(k)$. The other factors ($\hat{\boldsymbol{J}}_n$, etc.) are retained in their exact form.

Even if we cannot find $\zeta_{nn'}^{(j)}$ in closed form, we can evaluate its series easily (with rectangular grids), or more easily (in the general case), as will be shown below. For the example, considered in section 7, of rooftop basisfunctions (discontinuous in one direction and a discontiuous derivative in the other direction), the large k-behaviour of $\hat{\alpha}$ is typically given by $\hat{\alpha}_{nn'}^{(j)}(\boldsymbol{k}) = O(1/k_x^{2j}k_y)$. So we have improved the convergence of the $Z_{nn'}^{(j)}$-series to the order

$$O\Big(\frac{1}{(m_1^2+m_2^2)^{\frac{1}{2}N}m_1^{2j}m_2}\Big) \precsim O\Big(\frac{1}{|\boldsymbol{m}|^{N+1}}\Big), \tag{26}$$

where $N = 3$ (with a one-term expansion), or 5 (with a two-term expansion), or indeed as high as is available. For $N = 5$ we thus have for $Z_{nn'}$ a convergence rate $O(1/|\boldsymbol{m}|^6)$.

5 Evaluation of the asymptotic series $\zeta_{nn'}^{(j)}$

As we only rearranged the terms, series (25) is still slowly converging. Its simpler form, however, allows prospects of progress.

Inspired by Ewald's transformation, developed for similar problems [15, 12], we introduce the identity

$$\frac{1}{\mu^N} = \frac{2\lambda}{\Gamma(\frac{1}{2}N)}\int_0^\infty \rho^{\lambda N-1}\,\mathrm{e}^{-\mu^2\rho^{2\lambda}}\,\mathrm{d}\rho, \tag{27}$$

where λ is an arbitrary positive parameter (to be selected later), from which we have

$$\boxed{\begin{aligned}\frac{1}{k} &= \frac{2\lambda}{\sqrt{\pi}}\int_0^\infty \rho^{\lambda-1}\,\mathrm{e}^{-k^2\rho^{2\lambda}}\,\mathrm{d}\rho\\ \frac{1}{k^3} &= \frac{4\lambda}{\sqrt{\pi}}\int_0^\infty \rho^{3\lambda-1}\,\mathrm{e}^{-k^2\rho^{2\lambda}}\,\mathrm{d}\rho\end{aligned}}$$

and after changing the order of summation and integration, series (24) becomes

$$\zeta_{nn'}^{(j)} = \frac{2\lambda}{\sqrt{\pi}}\int_0^\infty \rho^{\lambda-1}\big(c_1^{(j)} + 2\rho^{2\lambda}c_2^{(j)}\big)\sum_{m_1=-\infty}^{\infty}\sum_{m_2=-\infty}^{\infty}\mathrm{e}^{-k^2\rho^{2\lambda}}\,\hat{\alpha}_{nn'}^{(j)}(\boldsymbol{k})\,\mathrm{d}\rho. \tag{29}$$

(Remember that $\boldsymbol{k} = B\boldsymbol{m} + \boldsymbol{k}_T^i$.) This expression (29) has the advantage that the series converges in m_1, m_2 exponentially fast, except near $\rho = 0$ where the series still needs a relatively large number of terms for convergence. As we will see below, this can be repaired by rewriting the series such that it converges again quickly when ρ is small. So the evaluation of the integrand will then consist of two parts: one, as equation 29, for an interval corresponding to large ρ, and one for an interval corresponding to small ρ.

In order to avoid evaluation at $\rho = 0$ we may select a λ larger than 1. This is not absolutely necessary, but it is convenient.

Also the integral in ρ converges exponentially at infinity (provided $k \neq 0$), and the integral can be evaluated numerically very efficiently. The infinite integration interval can be reduced to what is effectively a finite interval.

For later use it is convenient to introduce the couple

$$\hat{\epsilon}(\boldsymbol{k}, \rho) = \mathrm{e}^{-k^2\rho^{2\lambda}}, \tag{30a}$$

$$\epsilon(\boldsymbol{x}, \rho) = \frac{1}{4\pi^2}\iint_{-\infty}^{\infty} \hat{\epsilon}(\boldsymbol{k}, \rho)\, \mathrm{e}^{\mathrm{i}\boldsymbol{k}\cdot\boldsymbol{x}}\, \mathrm{d}\boldsymbol{k} = \frac{1}{4\pi\rho^{2\lambda}}\, \mathrm{e}^{-\frac{x^2}{4\rho^{2\lambda}}}, \tag{30b}$$

where $x = |\boldsymbol{x}|$ and $k = |\boldsymbol{k}|$.

6 A transformation for small ρ using Poisson's formula

We will now concentrate on the double summation in equation 29. As this is a problem, separate from the ρ-integration, we will simplify the notation, and write everywhere ρ, where we really mean ρ^{λ}.

6.1 Poisson's Formula

When $\boldsymbol{m}$ denotes a 2-dimensional index vector, and $\boldsymbol{\xi}$ denotes a 2-dimensional real variable, the function

$$\sum_{m_1=-\infty}^{\infty}\sum_{m_2=-\infty}^{\infty} \psi(\boldsymbol{m}+\boldsymbol{\xi})$$

is 1-periodic in $\boldsymbol{\xi}$ and can therefore be written as a Fourier double series

$$\sum_{m_1=-\infty}^{\infty}\sum_{m_2=-\infty}^{\infty} \psi(\boldsymbol{m}+\boldsymbol{\xi}) = \sum_{n_1=-\infty}^{\infty}\sum_{n_2=-\infty}^{\infty} \mathrm{e}^{2\pi\mathrm{i}\boldsymbol{n}\cdot\boldsymbol{\xi}} \int_0^1\int_0^1 \sum_{m_1=-\infty}^{\infty}\sum_{m_2=-\infty}^{\infty} \psi(\boldsymbol{m}+\boldsymbol{z})\, \mathrm{e}^{-2\pi\mathrm{i}\boldsymbol{n}\cdot\boldsymbol{z}}\, \mathrm{d}\boldsymbol{z}$$

$$= \sum_{n_1=-\infty}^{\infty}\sum_{n_2=-\infty}^{\infty} \mathrm{e}^{2\pi\mathrm{i}\boldsymbol{n}\cdot\boldsymbol{\xi}} \iint_{-\infty}^{\infty} \psi(\boldsymbol{z})\, \mathrm{e}^{-2\pi\mathrm{i}\boldsymbol{n}\cdot\boldsymbol{z}}\, \mathrm{d}\boldsymbol{z}.$$

In the last line we recognise the Fourier transform

$$\hat{\psi}(\boldsymbol{\kappa}) = \iint_{-\infty}^{\infty} \psi(\boldsymbol{z})\, \mathrm{e}^{-\mathrm{i}\boldsymbol{\kappa}\cdot\boldsymbol{z}}\, \mathrm{d}\boldsymbol{z}. \tag{31}$$

Hence, we obtain for $\boldsymbol{\xi} = 0$ the 2-dimensional form of Poisson's formula

$$\sum_{m_1=-\infty}^{\infty}\sum_{m_2=-\infty}^{\infty} \psi(\boldsymbol{m}) = \sum_{m_1=-\infty}^{\infty}\sum_{m_2=-\infty}^{\infty} \hat{\psi}(2\pi\boldsymbol{m}), \tag{32}$$

or in the inverse direction

$$\sum_{m_1=-\infty}^{\infty}\sum_{m_2=-\infty}^{\infty} \hat{\psi}(\boldsymbol{m}) = 4\pi^2 \sum_{m_1=-\infty}^{\infty}\sum_{m_2=-\infty}^{\infty} \psi(2\pi\boldsymbol{m}). \tag{33}$$

The functions we are actually dealing with, have a particular form as a function of $\boldsymbol{m}$, as they have the form $\hat{\psi}(\boldsymbol{m}) = \hat{\phi}(\boldsymbol{B}\boldsymbol{m} + \boldsymbol{k}_T^i)$. By using equation (17) for a co-ordinate transformation from $\boldsymbol{\kappa}$ to $\boldsymbol{k}$

$$\boldsymbol{k} = \boldsymbol{B}\boldsymbol{\kappa} + \boldsymbol{k}_T^i,\ \boldsymbol{\kappa} = \tfrac{1}{2\pi}\boldsymbol{A}^T(\boldsymbol{k} - \boldsymbol{k}_T^i),\ \mathrm{d}\boldsymbol{\kappa} = \tfrac{1}{4\pi^2}\det(\boldsymbol{A})\,\mathrm{d}\boldsymbol{k}, \tag{34}$$

we obtain

$$\begin{aligned}\sum_{m_1=-\infty}^{\infty}\sum_{m_2=-\infty}^{\infty}\hat{\phi}(\boldsymbol{B}\boldsymbol{m} + \boldsymbol{k}_T^i) &= \sum_{m_1=-\infty}^{\infty}\sum_{m_2=-\infty}^{\infty}\iint_{-\infty}^{\infty}\hat{\phi}(\boldsymbol{B}\boldsymbol{\kappa} + \boldsymbol{k}_T^i)\,\mathrm{e}^{2\pi\mathrm{i}\boldsymbol{m}\cdot\boldsymbol{\kappa}}\,\mathrm{d}\boldsymbol{\kappa}\\ &= \tfrac{1}{4\pi^2}\det(\boldsymbol{A})\sum_{m_1=-\infty}^{\infty}\sum_{m_2=-\infty}^{\infty}\mathrm{e}^{-\mathrm{i}\boldsymbol{A}\boldsymbol{m}\cdot\boldsymbol{k}_T^i}\iint_{-\infty}^{\infty}\hat{\phi}(\boldsymbol{k})\,\mathrm{e}^{\mathrm{i}\boldsymbol{A}\boldsymbol{m}\cdot\boldsymbol{k}}\,\mathrm{d}\boldsymbol{k}\\ &= \det(\boldsymbol{A})\sum_{m_1=-\infty}^{\infty}\sum_{m_2=-\infty}^{\infty}\mathrm{e}^{-\mathrm{i}\boldsymbol{A}\boldsymbol{m}\cdot\boldsymbol{k}_T^i}\,\phi(\boldsymbol{A}\boldsymbol{m}).\end{aligned} \tag{35}$$

For the double summation in (29) we have thus the result

$$\sum_{m_1=-\infty}^{\infty}\sum_{m_2=-\infty}^{\infty}\hat{\epsilon}(\boldsymbol{k},\rho)\hat{\alpha}_{nn'}^{(j)}(\boldsymbol{k}) = \det(\boldsymbol{A})\sum_{m_1=-\infty}^{\infty}\sum_{m_2=-\infty}^{\infty}\mathrm{e}^{-\mathrm{i}\boldsymbol{A}\boldsymbol{m}\cdot\boldsymbol{k}_T^i}\,\bar{\bar{\alpha}}_{nn'}^{(j)}(\boldsymbol{A}\boldsymbol{m},\rho), \tag{36}$$

where $\boldsymbol{k} = \boldsymbol{B}\boldsymbol{m} + \boldsymbol{k}_T^i$ and $\bar{\bar{\alpha}}_{nn'}^{(j)}(\boldsymbol{x},\rho)$ is the inverse Fourier transform of $\hat{\epsilon}(\boldsymbol{k},\rho)\hat{\alpha}_{nn'}^{(j)}(\boldsymbol{k})$. This result (36) is the key to our m_1, m_2-acceleration: the series at the left-hand side converge exponentially fast for large ρ, while the series at the right-hand side converge exponentially fast for small ρ, as will be shown in the following.

6.2 An exponential regularisation

The inverse transform $\bar{\bar{\alpha}}_{nn'}^{(j)}$ plays an important rôle in our analysis. It may be considered as a regularisation of $\alpha_{nn'}^{(j)}(\boldsymbol{x})$, with interesting properties. Therefore we will consider this regularisation in more detail.

Introduce the inverse Fourier transform $\bar{\bar{F}}(\boldsymbol{x},\rho)$ of $\hat{\epsilon}(\boldsymbol{k},\rho)\hat{F}(\boldsymbol{k})$, the exponentially smoothed Fourier transform of $F(\boldsymbol{x})$,

$$\bar{\bar{F}}(\boldsymbol{x},\rho) = \tfrac{1}{4\pi^2}\iint_{-\infty}^{\infty}\hat{F}(\boldsymbol{k})\,\mathrm{e}^{-k^2\rho^2}\,\mathrm{e}^{\mathrm{i}\boldsymbol{k}\cdot\boldsymbol{x}}\,\mathrm{d}\boldsymbol{k}. \tag{37a}$$

From the convolution theorem

$$\iint_{-\infty}^{\infty}f(\boldsymbol{x})g(\boldsymbol{x})\,\mathrm{e}^{-\mathrm{i}\boldsymbol{k}\cdot\boldsymbol{x}}\,\mathrm{d}\boldsymbol{x} = \frac{1}{4\pi^2}\iint_{-\infty}^{\infty}\hat{f}(\boldsymbol{v})\hat{g}(\boldsymbol{k}-\boldsymbol{v})\,\mathrm{d}\boldsymbol{v}, \tag{38a}$$

$$\iint_{-\infty}^{\infty}f(\boldsymbol{y})g(\boldsymbol{x}-\boldsymbol{y})\,\mathrm{d}\boldsymbol{y} = \frac{1}{4\pi^2}\iint_{-\infty}^{\infty}\hat{f}(\boldsymbol{k})\hat{g}(\boldsymbol{k})\,\mathrm{e}^{\mathrm{i}\boldsymbol{k}\cdot\boldsymbol{x}}\,\mathrm{d}\boldsymbol{k}, \tag{38b}$$

and equations (30) it transpires that this is equivalent to the convolution product

$$\bar{\bar{F}}(\boldsymbol{x},\rho) = \iint_{-\infty}^{\infty}\frac{1}{4\pi\rho^2}\exp\!\left(-\tfrac{|\boldsymbol{x}-\boldsymbol{y}|^2}{4\rho^2}\right)F(\boldsymbol{y})\,\mathrm{d}\boldsymbol{y}. \tag{37b}$$

Since

$$\iint_{-\infty}^{\infty} \frac{1}{4\pi\rho^2} \exp\!\left(-\tfrac{|\boldsymbol{x}-\boldsymbol{y}|^2}{4\rho^2}\right) \mathrm{d}\boldsymbol{y} = 1,$$

$\bar{\bar{F}}$ may be considered [7] as an infinite differentiable regularisation of the (possibly generalised) function F, such that $\bar{\bar{F}}(\boldsymbol{x}, 0) = F(\boldsymbol{x})$. If F has bounded support (the usual case in our application of basis functions), $\bar{\bar{F}}(\boldsymbol{x}, \rho)$ decays (in $\boldsymbol{x}$) exponentially to zero outside the region where $F \neq 0$.

By noting that $\bar{\bar{F}}$ satisfies

$$\nabla_x^2 \bar{\bar{F}}(\boldsymbol{x}, \rho) = \frac{\partial}{\partial\rho^2} \bar{\bar{F}}(x, \rho),$$

$\bar{\bar{F}}$ may also be considered as a solution of the heat equation, if we identify ρ^2 to a time-like variable. $\bar{\bar{F}}(\boldsymbol{x}, \rho)$ is the temperature profile after a time ρ^2 of the initial profile $\bar{\bar{F}}(\boldsymbol{x}, 0) = F(\boldsymbol{x})$.

The corresponding formula's in 1D are

$$\bar{\bar{F}}(x, \rho) = \tfrac{1}{2\pi} \int_{-\infty}^{\infty} \hat{F}(\kappa)\, \mathrm{e}^{-\kappa^2\rho^2}\, \mathrm{e}^{\mathrm{i}\kappa x}\ \mathrm{d}\kappa \tag{39a}$$

$$= \int_{-\infty}^{\infty} \frac{1}{\sqrt{4\pi\rho^2}} \exp\!\left(-\tfrac{(x-y)^2}{4\rho^2}\right) F(y)\, \mathrm{d}y. \tag{39b}$$

6.3 The final result

Altogether we have now a part for large ρ and one for small ρ. When a suitable transition point is, say, $\rho = \rho_1$, we obtain for equation (29) the following expression, where both the summation converges exponentially in $\boldsymbol{m}$ for all ρ, and the integral converges exponentially in ρ:

$$\begin{aligned}
\zeta_{nn'}^{(j)} = \frac{2\lambda}{\sqrt{\pi}} \Bigg\{ & \det(\boldsymbol{A}) \cdot \\
\cdot \int_0^{\rho_1} & \rho^{\lambda-1} \left(c_1^{(j)} + 2\rho^{2\lambda} c_2^{(j)}\right) \sum_{m_1=-\infty}^{\infty} \sum_{m_2=-\infty}^{\infty} \mathrm{e}^{-\mathrm{i}\boldsymbol{A}\boldsymbol{m}\cdot\boldsymbol{k}_T^i}\, \bar{\bar{\alpha}}_{nn'}^{(j)}(\boldsymbol{A}\boldsymbol{m}, \rho)\, \mathrm{d}\rho + \\
+ \int_{\rho_1}^{\infty} & \rho^{\lambda-1} \left(c_1^{(j)} + 2\rho^{2\lambda} c_2^{(j)}\right) \sum_{m_1=-\infty}^{\infty} \sum_{m_2=-\infty}^{\infty} \hat{\epsilon}(\boldsymbol{k}, \rho) \hat{\alpha}_{nn'}^{(j)}(\boldsymbol{k}, \rho)\, \mathrm{d}\rho \Bigg\} \\
& \text{(where } \boldsymbol{k} = \boldsymbol{B}\boldsymbol{m} + \boldsymbol{k}_T^i\text{).}
\end{aligned} \tag{40}$$

For small ρ the function ϵ behaves like a δ-function and filters out in equation (37b) the neighbourhood of $\boldsymbol{y} = \boldsymbol{x}$, such that we have for any reasonable $\alpha_{nn'}^{(j)}$ approximately

$$\bar{\bar{\alpha}}_{nn'}^{(j)}(\boldsymbol{x}, \rho) \simeq \iint_{-\infty}^{\infty} \epsilon(\boldsymbol{y}, \rho) \left(\alpha_{nn'}^{(j)}(\boldsymbol{x}) + \dots\right) \mathrm{d}\boldsymbol{y} = \alpha_{nn'}^{(j)}(\boldsymbol{x}) + \dots \qquad (\rho \downarrow 0). \tag{41}$$

This shows why the transformed series (36) is now more and more exponentially converging for smaller ρ. Since $\alpha^{(j)}_{nn'}$ has compact support, $\bar{\bar{\alpha}}^{(j)}_{nn'}$ has an "almost" compact support while it vanishes exponentially for large values of the argument.

The remaining problem is now to find in any particular case the inverse Fourier transform $\bar{\bar{\alpha}}$. In general an analytical expression appears to be difficult. A numerical FFT-approach is straightforward and fast – at least, for each triple (ρ, n, n') – and may be a worthwhile option.

Considerable progress can be made if the basis function are chosen on an orthogonal grid, such that their x and y dependence becomes separable. For sufficiently simple basis functions the integral (37a) defining $\bar{\bar{\alpha}}^{(j)}_{nn'}$ can be evaluated explicitly. We will see below an example of this type.

7 Rooftop basis functions

7.1 Analysis

In the following we will consider in detail some applications consisting of rectangular geometries (strip, square, gridded square), where the basis and test functions are rooftop functions, with orientation $\boldsymbol{d}$ in either x or y direction (figure 3). We introduce the generic basis functions $\mathcal{J}$ and test functions $\mathcal{K}$

$$\mathcal{J}(\boldsymbol{x}; \boldsymbol{x}_0, \boldsymbol{d}, a, b, w) = \boldsymbol{d}\, \Pi\big((\boldsymbol{u}_z \times \boldsymbol{d}) \cdot (\boldsymbol{x} - \boldsymbol{x}_0); w\big)\, \Lambda\big(\boldsymbol{d} \cdot (\boldsymbol{x} - \boldsymbol{x}_0); a, b\big), \tag{42}$$

$$\mathcal{K}(\boldsymbol{x}; \boldsymbol{x}_0, \boldsymbol{d}, a, b) = \boldsymbol{d}\, \delta\big((\boldsymbol{u}_z \times \boldsymbol{d}) \cdot (\boldsymbol{x} - \boldsymbol{x}_0)\big)\, \Lambda\big(\boldsymbol{d} \cdot (\boldsymbol{x} - \boldsymbol{x}_0); a, b\big), \tag{43}$$

where $\boldsymbol{d} \in \{\boldsymbol{u}_x, \boldsymbol{u}_y\}$, and

$$\Lambda(x; a, b) = \begin{cases} 1 + x/a & \text{for} \quad x \in [-a, 0] \\ 1 - x/b & \text{for} \quad x \in [0, b] \\ 0 & \text{otherwise,} \end{cases} \tag{44}$$

$$\Pi(x; w) = \begin{cases} w^{-1} & \text{for} \quad x \in [-\tfrac{1}{2}w, \tfrac{1}{2}w] \\ 0 & \text{otherwise.} \end{cases} \tag{45}$$

Results seem to be numerically optimal if $a \simeq b \simeq w$.

The support S_0 is the following rectangle

$$S = \boldsymbol{x}_0 + \begin{cases} [-a, b] \times [-\tfrac{1}{2}w, \tfrac{1}{2}w] & \text{if} \quad \boldsymbol{d} = \boldsymbol{u}_x, \\ [-\tfrac{1}{2}w, \tfrac{1}{2}w] \times [-a, b] & \text{if} \quad \boldsymbol{d} = \boldsymbol{u}_y. \end{cases} \tag{46}$$

The Fourier transforms are

$$\hat{\mathcal{J}}(\boldsymbol{k}; \boldsymbol{x}_0, \boldsymbol{d}, a, b, w) = \boldsymbol{d}\, \mathrm{e}^{-\mathrm{i}\boldsymbol{k}\cdot\boldsymbol{x}_0}\, \hat{\Pi}\big((\boldsymbol{u}_z \times \boldsymbol{d}) \cdot \boldsymbol{k}; w\big)\, \hat{\Lambda}\big(\boldsymbol{d} \cdot \boldsymbol{k}; a, b\big), \tag{47}$$

$$\hat{\mathcal{K}}(\boldsymbol{k}; \boldsymbol{x}_0, \boldsymbol{d}, a, b) = \boldsymbol{d}\, \mathrm{e}^{-\mathrm{i}\boldsymbol{k}\cdot\boldsymbol{x}_0}\, \hat{\Lambda}\big(\boldsymbol{d} \cdot \boldsymbol{k}; a, b\big), \tag{48}$$

where

$$\mathcal{S}(z) = \frac{\sin \frac{1}{2}z}{\frac{1}{2}z} \tag{49}$$

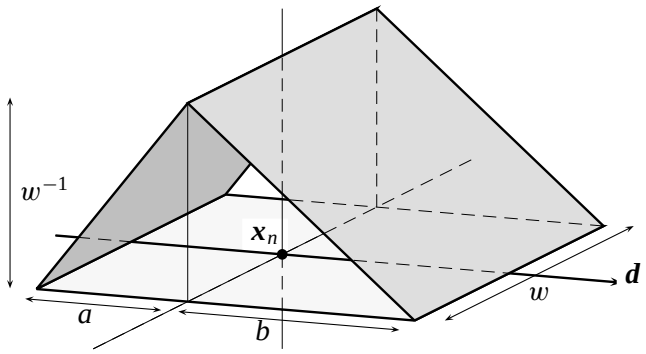

Figure 3: Definition sketch of the rooftop basis function.

$$\mathcal{T}(z) = \mathcal{S}(2z) + \tfrac{1}{2}\mathrm{i}z\mathcal{S}(z)^2 = \mathcal{S}(z)\,\mathrm{e}^{\frac{1}{2}\mathrm{i}z} \tag{50}$$

$$\hat{\Lambda}(k;a,b) = \frac{\mathcal{T}(ka) - \mathcal{T}(-kb)}{\mathrm{i}k}, \tag{51}$$

$$\hat{\Pi}(k;w) = \mathcal{S}(kw). \tag{52}$$

Note that

$$\Lambda(-x;a,b) = \Lambda(x;b,a), \quad \hat{\Lambda}(0;a,b) = \tfrac{1}{2}(a+b),$$
$$\hat{\Lambda}(-k;a,b) = \hat{\Lambda}(k;a,b)^* = \hat{\Lambda}(k;b,a),$$
$$\mathcal{T}(z)^* = \mathcal{T}(-z), \quad \hat{\Lambda}(k;a,a) = a\mathcal{S}(ka)^2,$$

while both Π and $\hat{\Pi}$ are symmetric.

It follows that (see equation 10)

$$V_0 = -(\boldsymbol{d}\cdot\hat{\boldsymbol{E}}_T^{pl})\,\mathrm{e}^{\mathrm{i}\boldsymbol{k}_T^i\cdot\boldsymbol{x}_0}\,\hat{\Lambda}(-\boldsymbol{d}\cdot\boldsymbol{k}_T^i;a,b), \tag{53}$$

while $V_0 = -\frac{1}{2}(a+b)(\boldsymbol{d}\cdot\hat{\boldsymbol{E}}_T^{pl})\,\mathrm{e}^{\mathrm{i}\boldsymbol{k}_T^i\cdot\boldsymbol{x}_0}$ if $(\boldsymbol{d}\cdot\boldsymbol{k}_T^i) = 0$.

The coupling terms between a test function $\mathcal{K}(\boldsymbol{x};\boldsymbol{x}_0,\boldsymbol{d},a,b)$ and a basis function $\mathcal{J}(\boldsymbol{x};\boldsymbol{y}_0,\boldsymbol{e},p,q,w)$ become now

$$\hat{\alpha}^{(1)}_{\boldsymbol{x}_0\boldsymbol{y}_0}(\boldsymbol{k}) = \mathrm{e}^{\mathrm{i}\boldsymbol{k}\cdot(\boldsymbol{x}_0-\boldsymbol{y}_0)}\,\mathcal{S}\big((\boldsymbol{u}_z\times\boldsymbol{e})\cdot\boldsymbol{k}w\big)$$
$$\big(\mathcal{T}(-\boldsymbol{k}\cdot\boldsymbol{d}a) - \mathcal{T}(\boldsymbol{k}\cdot\boldsymbol{d}b)\big)\big(\mathcal{T}(\boldsymbol{k}\cdot\boldsymbol{e}p) - \mathcal{T}(-\boldsymbol{k}\cdot\boldsymbol{e}q)\big), \tag{54a}$$

$$\hat{\alpha}^{(2)}_{\boldsymbol{x}_0\boldsymbol{y}_0}(\boldsymbol{k}) = (\boldsymbol{d}\cdot\boldsymbol{e})\,\mathrm{e}^{\mathrm{i}\boldsymbol{k}\cdot(\boldsymbol{x}_0-\boldsymbol{y}_0)}\,\mathcal{S}\big((\boldsymbol{u}_z\times\boldsymbol{e})\cdot\boldsymbol{k}w\big)$$
$$\Big(\frac{\mathcal{T}(-\boldsymbol{k}\cdot\boldsymbol{d}a) - \mathcal{T}(\boldsymbol{k}\cdot\boldsymbol{d}b)}{\boldsymbol{k}\cdot\boldsymbol{d}}\Big)\Big(\frac{\mathcal{T}(\boldsymbol{k}\cdot\boldsymbol{e}p) - \mathcal{T}(-\boldsymbol{k}\cdot\boldsymbol{e}q)}{\boldsymbol{k}\cdot\boldsymbol{e}}\Big). \tag{54b}$$

7.2 Auxiliary functions

Introduce the following auxiliary functions

$$f_0(z) = \tfrac{1}{2\sqrt{\pi}}\,\mathrm{e}^{-Z^2} \tag{55a}$$

$$f_1(z) = -\tfrac{1}{2}\,\mathrm{erfc}(Z) \tag{55b}$$

$$f_2(z) = \tfrac{1}{\sqrt{\pi}}\,\mathrm{e}^{-Z^2} - Z\,\mathrm{erfc}(Z) \tag{55c}$$

$$f_3(z) = \tfrac{1}{\sqrt{\pi}}\,Z\,\mathrm{e}^{-Z^2} - (Z^2+\tfrac{1}{2})\,\mathrm{erfc}(Z) \tag{55d}$$

$$f_4(z) = \tfrac{2}{3\sqrt{\pi}}(Z^2+1)\,\mathrm{e}^{-Z^2} - Z(\tfrac{2}{3}Z^2+1)\,\mathrm{erfc}(Z) \tag{55e}$$

where $Z = \frac{1}{2}z$. Note that $f_n' = f_{n-1}$. The functions are related to the repeated integrals $\mathrm{i}^n\,\mathrm{erfc}(z)$ of the complementary error function $\mathrm{erfc}(z)$ [6, 7.2] as follows (be aware of the confusing symbolism)

$$f_n(z) = (-2)^{n-2}\,\mathrm{i}^{n-1}\mathrm{erfc}(\tfrac{1}{2}z) = (-2)^{n-2}\,\mathrm{erfc}(n-1, \tfrac{1}{2}z).$$

Define the occurring combinations of $\mathcal{S}$ and $\mathcal{T}$ (see figures 4)

$$\hat{F}_1(\kappa;\, w) = \mathcal{S}(\kappa w) \tag{56a}$$

$$\hat{F}_2(\kappa;\, p, q) = \mathcal{T}(\kappa p) - \mathcal{T}(-\kappa q) \tag{56b}$$

$$\hat{F}_3(\kappa;\, w, a, b) = \mathcal{S}(\kappa w)\big(\mathcal{T}(-\kappa a) - \mathcal{T}(\kappa b)\big) \tag{56c}$$

$$\hat{F}_4(\kappa;\, a, b, p, q) = \big(\mathcal{T}(-\kappa a) - \mathcal{T}(\kappa b)\big)\big(\mathcal{T}(\kappa p) - \mathcal{T}(-\kappa q)\big) \tag{56d}$$

$$\hat{F}_5(\kappa;\, a, b, p, q) = \kappa^{-2}\big(\mathcal{T}(-\kappa a) - \mathcal{T}(\kappa b)\big)\big(\mathcal{T}(\kappa p) - \mathcal{T}(-\kappa q)\big) \tag{56e}$$

Special cases of some interest are

$$\hat{F}_2(\kappa;\, p, p) = \mathrm{i}\kappa p\,\mathcal{S}(\kappa p)^2, \qquad \hat{F}_3(\kappa;\, w, a, a) = -\mathrm{i}\kappa a\,\mathcal{S}(\kappa a)^2\,\mathcal{S}(\kappa w)$$
$$\hat{F}_4(\kappa;\, a, a, a, a) = (\kappa a)^2\,\mathcal{S}(\kappa a)^4, \qquad \hat{F}_5(\kappa;\, a, a, a, a) = a^2\,\mathcal{S}(\kappa a)^4$$
$$\hat{F}_5(0;\, a, b, p, q) = \tfrac{1}{4}(a+b)(p+q)$$

Noting the shift property

$$\tfrac{1}{2\pi}\int_{-\infty}^{\infty} \hat{F}_n(\kappa)\,\mathrm{e}^{\mathrm{i}\nu\kappa}\,\mathrm{e}^{-\kappa^2\rho^2}\,\mathrm{e}^{\mathrm{i}\kappa x}\,\mathrm{d}\kappa = \bar{\bar{F}}_n(x+\nu, \rho), \tag{57}$$

we have now explicitly

$$\bar{\bar{F}}_1(x, \rho;\, w) = \tfrac{1}{w}\Big\{ f_1\big(\tfrac{x+\frac{1}{2}w}{\rho}\big) - f_1\big(\tfrac{x-\frac{1}{2}w}{\rho}\big)\Big\} \tag{58a}$$

$$\bar{\bar{F}}_2(x, \rho;\, p, q) = -\big(\tfrac{1}{p}+\tfrac{1}{q}\big) f_1\big(\tfrac{x}{\rho}\big) + \tfrac{1}{p} f_1\big(\tfrac{x+p}{\rho}\big) + \tfrac{1}{q} f_1\big(\tfrac{x-q}{\rho}\big) \tag{58b}$$

$$\begin{aligned}\bar{\bar{F}}_3(x, \rho;\, w, a, b) = \tfrac{\rho}{w}\Big\{ &\big(\tfrac{1}{a}+\tfrac{1}{b}\big) f_2\big(\tfrac{x+\frac{1}{2}w}{\rho}\big) - \tfrac{1}{a} f_2\big(\tfrac{x+\frac{1}{2}w-a}{\rho}\big) - \tfrac{1}{b} f_2\big(\tfrac{x+\frac{1}{2}w+b}{\rho}\big)\\ &- \big(\tfrac{1}{a}+\tfrac{1}{b}\big) f_2\big(\tfrac{x-\frac{1}{2}w}{\rho}\big) + \tfrac{1}{a} f_2\big(\tfrac{x-\frac{1}{2}w-a}{\rho}\big) + \tfrac{1}{b} f_2\big(\tfrac{x-\frac{1}{2}w+b}{\rho}\big)\Big\}\end{aligned} \tag{58c}$$

$$\begin{aligned}\bar{\bar{F}}_4(x, \rho;\, a, b, p, q) = -\rho\Big\{ &\big(\tfrac{1}{p}+\tfrac{1}{q}\big)\big[\big(\tfrac{1}{a}+\tfrac{1}{b}\big) f_2(\tfrac{x}{\rho}) - \tfrac{1}{a} f_2(\tfrac{x-a}{\rho}) - \tfrac{1}{b} f_2(\tfrac{x+b}{\rho})\big]\\ &- \tfrac{1}{p}\big[\big(\tfrac{1}{a}+\tfrac{1}{b}\big) f_2(\tfrac{x+p}{\rho}) - \tfrac{1}{a} f_2(\tfrac{x+p-a}{\rho}) - \tfrac{1}{b} f_2(\tfrac{x+p+b}{\rho})\big]\\ &- \tfrac{1}{q}\big[\big(\tfrac{1}{a}+\tfrac{1}{b}\big) f_2(\tfrac{x-q}{\rho}) - \tfrac{1}{a} f_2(\tfrac{x-q-a}{\rho}) - \tfrac{1}{b} f_2(\tfrac{x-q+b}{\rho})\big]\Big\}\end{aligned} \tag{58d}$$

$$\begin{aligned}\bar{\bar{F}}_5(x, \rho;\, a, b, p, q) = \rho^3\Big\{ &(\tfrac{1}{p}+\tfrac{1}{q})\big[\big(\tfrac{1}{a}+\tfrac{1}{b}\big) f_4(\tfrac{x}{\rho}) - \tfrac{1}{a} f_4(\tfrac{x-a}{\rho}) - \tfrac{1}{b} f_4(\tfrac{x+b}{\rho})\big]\\ &- \tfrac{1}{p}\big[\big(\tfrac{1}{a}+\tfrac{1}{b}\big) f_4(\tfrac{x+p}{\rho}) - \tfrac{1}{a} f_4(\tfrac{x+p-a}{\rho}) - \tfrac{1}{b} f_4(\tfrac{x+p+b}{\rho})\big]\\ &- \tfrac{1}{q}\big[\big(\tfrac{1}{a}+\tfrac{1}{b}\big) f_4(\tfrac{x-q}{\rho}) - \tfrac{1}{a} f_4(\tfrac{x-q-a}{\rho}) - \tfrac{1}{b} f_4(\tfrac{x-q+b}{\rho})\big]\Big\}\end{aligned} \tag{58e}$$

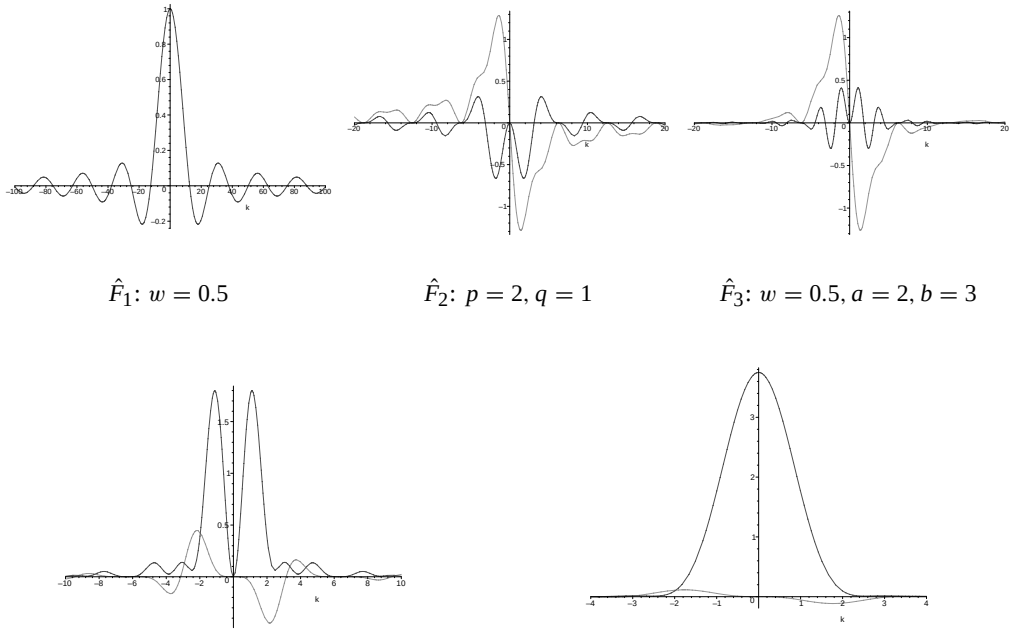

$\hat{F}_1$: $w = 0.5$ $\hat{F}_2$: $p = 2, q = 1$ $\hat{F}_3$: $w = 0.5, a = 2, b = 3$

$\hat{F}_4$: $a = 2, b = 3,\ p = 1, q = 2$ $\hat{F}_5$: $a = 2, b = 3,\ p = 1, q = 2$

Figure 4: Plots of $\hat{F}_n(k; ..)$. Note the slow decay.

Note that $\overline{\overline{F}}_n(x, 0; ..) = F_n(x; ..)$, the inverse Fourier transform of $\hat{F}_n(x; ..)$, is finite and only non-zero within a finite interval (related to the supports of $\Lambda(x; a, b)$ and $\Pi(x; w)$). For $\rho = 0$, $\overline{\overline{F}}_1$ describes a simple block, $\overline{\overline{F}}_2$ a double block, $\overline{\overline{F}}_3$ a double block with sides of finite slope, $\overline{\overline{F}}_4$ is a partwise linear function, and $\overline{\overline{F}}_5$ is a partwise quadratic function (figure 5).

7.3 Tables

From the above definitions (56), we can derive the table

$\boldsymbol{d}$	$\boldsymbol{e}$	$\hat{\alpha}^{(1)}_{\boldsymbol{x}_0\boldsymbol{y}_0}(\boldsymbol{k})$
x	x	$e^{i\boldsymbol{k}\cdot(\boldsymbol{x}_0-\boldsymbol{y}_0)}\ \hat{F}_1(k_y; w) \quad \hat{F}_4(k_x; a, b, p, q)$
y	y	$e^{i\boldsymbol{k}\cdot(\boldsymbol{x}_0-\boldsymbol{y}_0)}\ \hat{F}_1(k_x; w) \quad \hat{F}_4(k_y; a, b, p, q)$
x	y	$e^{i\boldsymbol{k}\cdot(\boldsymbol{x}_0-\boldsymbol{y}_0)}\ \hat{F}_2(k_y; p, q)\hat{F}_3(k_x; w, a, b)$
y	x	$e^{i\boldsymbol{k}\cdot(\boldsymbol{x}_0-\boldsymbol{y}_0)}\ \hat{F}_2(k_x; p, q)\hat{F}_3(k_y; w, a, b)$

while the non-zero results for $\hat{\alpha}^{(2)}_{\boldsymbol{x}_0\boldsymbol{y}_0}(\boldsymbol{k})$ are

$\boldsymbol{d}$	$\boldsymbol{e}$	$\hat{\alpha}^{(2)}_{\boldsymbol{x}_0\boldsymbol{y}_0}(\boldsymbol{k})$
x	x	$e^{i\boldsymbol{k}\cdot(\boldsymbol{x}_0-\boldsymbol{y}_0)}\ \hat{F}_1(k_y; w)\hat{F}_5(k_x; a, b, p, q)$
y	y	$e^{i\boldsymbol{k}\cdot(\boldsymbol{x}_0-\boldsymbol{y}_0)}\ \hat{F}_1(k_x; w)\hat{F}_5(k_y; a, b, p, q)$

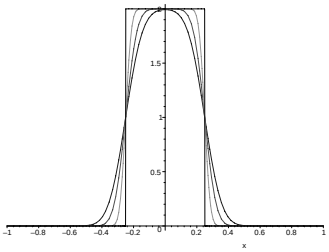

$\bar{\bar{F}}_1$: $w = 0.5$

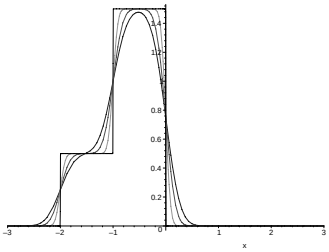

$\bar{\bar{F}}_2$: $p = 2, q = 1$

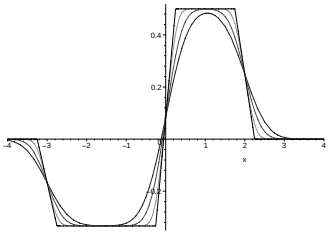

$\bar{\bar{F}}_3$: $w = 0.5, a = 2, b = 3$

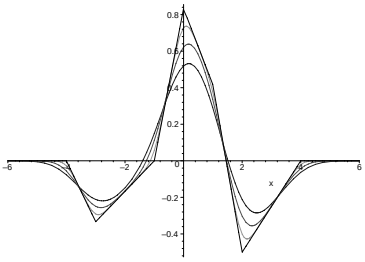

$\bar{\bar{F}}_4$: $a = 2, b = 3,\ p = 1, q = 2$

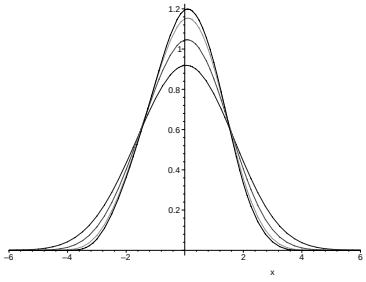

$\bar{\bar{F}}_5$: $a = 2, b = 3,\ p = 1, q = 2$

Figure 5: Plots of $\bar{\bar{F}}_n(x, \rho; ..)$ in x for various ρ. Note the fast decay.

The corresponding transforms $\bar{\bar{\alpha}}^{(1)}_{\boldsymbol{x}_0\boldsymbol{y}_0}(\boldsymbol{x}, \rho)$ are, with definitions (58) and shift property (57), in table form (where $\boldsymbol{X} = (X, Y) = \boldsymbol{x} + \boldsymbol{x}_0 - \boldsymbol{y}_0$)

d	***e***	$\bar{\bar{\alpha}}^{(1)}_{\boldsymbol{x}_0\boldsymbol{y}_0}(\boldsymbol{x}, \rho)$
x	x	$\bar{\bar{F}}_1(Y, \rho; w) \quad \bar{\bar{F}}_4(X, \rho; a, b, p, q)$
y	y	$\bar{\bar{F}}_1(X, \rho; w) \quad \bar{\bar{F}}_4(Y, \rho; a, b, p, q)$
x	y	$\bar{\bar{F}}_2(Y, \rho; p, q)\bar{\bar{F}}_3(X, \rho; w, a, b)$
y	x	$\bar{\bar{F}}_2(X, \rho; p, q)\bar{\bar{F}}_3(Y, \rho; w, a, b)$

while the non-zero results of $\bar{\bar{\alpha}}^{(2)}_{\boldsymbol{x}_0\boldsymbol{y}_0}(\boldsymbol{x}, \rho)$ are

d	***e***	$\bar{\bar{\alpha}}^{(2)}_{\boldsymbol{x}_0\boldsymbol{y}_0}(\boldsymbol{x}, \rho)$
x	x	$\bar{\bar{F}}_1(Y, \rho; w)\bar{\bar{F}}_5(X, \rho; a, b, p, q)$
y	y	$\bar{\bar{F}}_1(X, \rho; w)\bar{\bar{F}}_5(Y, \rho; a, b, p, q)$

As long as $\lambda > 1$ the singular behaviour at $\rho = 0$ can be ignored.

8 The strip

For the typical example of a strip of width w and length L at $\boldsymbol{x} = \boldsymbol{x}_0$, oriented in x-direction and subdivided into N_{side} subsections of length Δ, where $\Delta = L/N_{\text{side}}$,

$x_n = x_0 + n\Delta$, $\boldsymbol{x}_n = x_n\boldsymbol{u}_x + y_0\boldsymbol{u}_y$, $n = 0 \ldots N_{\text{side}}$ (figure 6), the $N = N_{\text{side}} - 1$ basis $(\boldsymbol{J}_n)$ and test functions $(\boldsymbol{K}_n)$ are chosen as follows

$$\boldsymbol{J}_n(\boldsymbol{r}_T) = \mathcal{J}(\boldsymbol{x}; \boldsymbol{x}_n, \boldsymbol{u}_x, \Delta, \Delta, w), \tag{59a}$$

$$\boldsymbol{K}_n(\boldsymbol{r}_T) = \mathcal{K}(\boldsymbol{x}; \boldsymbol{x}_n, \boldsymbol{u}_x, \Delta, \Delta), \tag{59b}$$

where $n = 1, \ldots, N$. Note that the end points $\boldsymbol{x}_0, \boldsymbol{x}_{N_{\text{side}}}$ are no nodes of the basis functions.

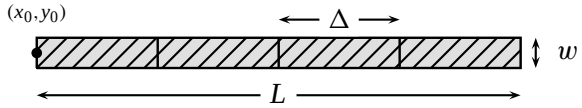

Figure 6: Definition sketch of the strip ($N = 3$).

The source term is then

$$V_n = -(\boldsymbol{u}_x \cdot \hat{\boldsymbol{E}}_T^{pl})\Delta\, \mathrm{e}^{\mathrm{i}\boldsymbol{k}_T^i \cdot \boldsymbol{x}_n}\, \mathcal{S}(\Delta k_x^i)^2, \tag{60}$$

while

$$\big[-\mathrm{i}\boldsymbol{k}\cdot\hat{\boldsymbol{K}}_n^*(\boldsymbol{k})\big]\big[\mathrm{i}\boldsymbol{k}\cdot\hat{\boldsymbol{J}}_{n'}(\boldsymbol{k})\big] = \hat{\alpha}_{nn'}^{(1)}(\boldsymbol{k}) = k_x^2\Delta^2\mathcal{S}(k_x\Delta)^4\mathcal{S}(k_y w)\,\mathrm{e}^{\mathrm{i}k_x(n-n')\Delta} \tag{61a}$$

$$\big[\hat{\boldsymbol{K}}_n^*(\boldsymbol{k})\cdot\hat{\boldsymbol{J}}_{n'}(\boldsymbol{k})\big] = \hat{\alpha}_{nn'}^{(2)}(\boldsymbol{k}) = \Delta^2\mathcal{S}(k_x\Delta)^4\mathcal{S}(k_y w)\,\mathrm{e}^{\mathrm{i}k_x(n-n')\Delta} \tag{61b}$$

and so we have with definitions (56)

$$\hat{\alpha}_{nn'}^{(1)}(\boldsymbol{k}, \rho) = \mathrm{e}^{\mathrm{i}(n-n')k_x\Delta}\,\hat{F}_1(k_y, w)\hat{F}_4(k_x, \Delta, \Delta, \Delta, \Delta) \tag{62a}$$

$$\hat{\alpha}_{nn'}^{(2)}(\boldsymbol{k}, \rho) = \mathrm{e}^{\mathrm{i}(n-n')k_x\Delta}\,\hat{F}_1(k_y, w)\hat{F}_5(k_x, \Delta, \Delta, \Delta, \Delta). \tag{62b}$$

Using (37,57,58) we find the regularisations of $\alpha_{nn'}^{(j)}(\boldsymbol{x})$

$$\bar{\bar{\alpha}}_{nn'}^{(1)}(\boldsymbol{x}, \rho) = \bar{\bar{F}}_1\big(Y, \rho, w\big)\bar{\bar{F}}_4\big(X, \rho, \Delta, \Delta, \Delta, \Delta\big) \tag{63a}$$

$$\bar{\bar{\alpha}}_{nn'}^{(2)}(\boldsymbol{x}, \rho) = \bar{\bar{F}}_1\big(Y, \rho, w\big)\bar{\bar{F}}_5\big(X, \rho, \Delta, \Delta, \Delta, \Delta\big) \tag{63b}$$

(where $X = x + n\Delta - n'\Delta$ and $Y = y + n\Delta - n'\Delta$) altogether to be substituted into formula (40). Efficient programming should utilize the fact that the results only depend on $n - n'$.

8.1 The orthogonal array

If the lattice is orthogonal, k_x only depends on m_1 and k_y only on m_2. Since $\hat{\alpha}_{nn'}^{(j)}(\boldsymbol{k})$ and $\hat{\epsilon}(\boldsymbol{k}, \rho)$ can exactly be factored in their k_x and k_y dependence, the summation over m_1 and m_2 can be decoupled.

Note that if $n - n' = 0$ the result is real, while the results for $n - n' > 0$ immediately imply the results for $n - n' < 0$ by complex conjugation.

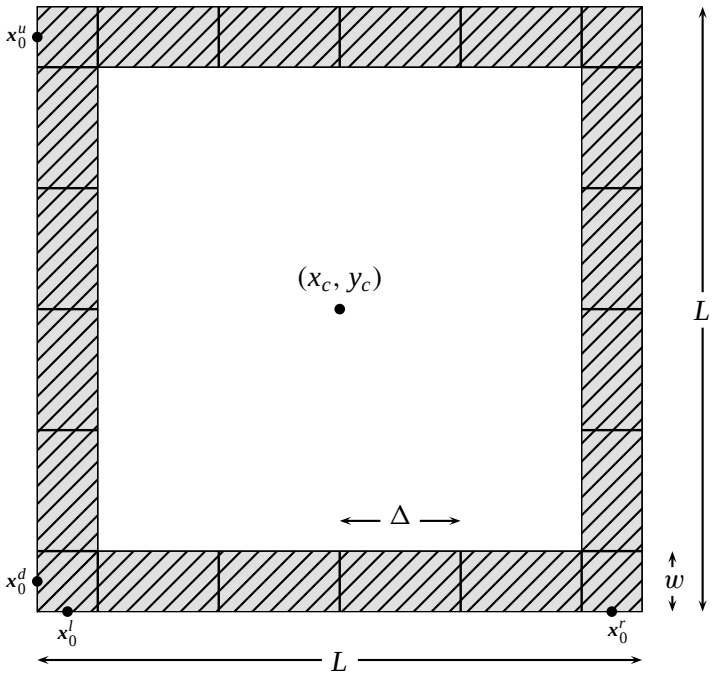

Figure 7: Definition sketch of the square ($N = 4 \times 5 = 20$)

9 The square

Consider the square as given in figure 7. The sides of the square, measured along the outside boundaries, are of length L. Each side has width w, where and $w/L \ll 1$. The square is centred at coordinate x_c, y_c. The square is described by 4 strips of size $L \times w$, as introduced above in section 8, and given in figure 7. Each strip is subdivided in its axial direction into N_{side} subsections Δ_n: at the ends we have 2 of length w: $\Delta_1 = \Delta_{N_{\text{side}}} = w$, and in the middle we have $N_{\text{side}} - 2$ of length $\Delta_n = (L - 2w)/(N_{\text{side}} - 2)$.

At each side, $N_1 = N_{\text{side}} - 1$ basis and test functions are defined, similar to what is introduced in section 8, and oriented co-axial with the strip. The basis and testfunctions count from $n = 1$ to $N = 4N_1$, in positive x, respectively positive y direction, starting from the lower left corner, via the *down* side, the *right* and *upper* side to the *left* side.

We have for the reference points (positioned along the centerlines):

$$\begin{aligned}
\boldsymbol{x}_0^d &= (x_c - \tfrac{1}{2}L \qquad)\boldsymbol{u}_x + (y_c - \tfrac{1}{2}L + \tfrac{1}{2}w)\boldsymbol{u}_y, \\
\boldsymbol{x}_0^r &= (x_c + \tfrac{1}{2}L - \tfrac{1}{2}w)\boldsymbol{u}_x + (y_c - \tfrac{1}{2}L \qquad)\boldsymbol{u}_y, \\
\boldsymbol{x}_0^u &= (x_c - \tfrac{1}{2}L \qquad)\boldsymbol{u}_x + (y_c + \tfrac{1}{2}L - \tfrac{1}{2}w)\boldsymbol{u}_y, \\
\boldsymbol{x}_0^l &= (x_c - \tfrac{1}{2}L + \tfrac{1}{2}w)\boldsymbol{u}_x + (y_c - \tfrac{1}{2}L \qquad)\boldsymbol{u}_y.
\end{aligned}$$

The source vector, the nodes, and basis and test functions are given for the **down** side, where $n = 1 \ldots N_1$, $n_d = n$, $\boldsymbol{d} = \boldsymbol{u}_x$:

$$\boldsymbol{x}_n = \boldsymbol{x}_0^d + \boldsymbol{u}_x \sum_{i=1}^{n_d} \Delta_i \tag{64a}$$

$$V_n = (\boldsymbol{u}_x \cdot \hat{\boldsymbol{E}}_T^{pl})\, \mathrm{e}^{\mathrm{i}\boldsymbol{k}_T^i \cdot \boldsymbol{x}_n} (\mathrm{i}k_x^i)^{-1} \big(\mathcal{T}(-k_x^i \Delta_{n_d}) - \mathcal{T}(k_x^i \Delta_{n_d+1})\big) \tag{64b}$$

$$\boldsymbol{J}_n(\boldsymbol{r}_T) = \mathcal{J}(\boldsymbol{x}; \boldsymbol{x}_n, \boldsymbol{u}_x, \Delta_{n_d}, \Delta_{n_d+1}, w), \tag{64c}$$

$$\boldsymbol{K}_n(\boldsymbol{r}_T) = \mathcal{K}(\boldsymbol{x}; \boldsymbol{x}_n, \boldsymbol{u}_x, \Delta_{n_d}, \Delta_{n_d+1}), \tag{64d}$$

the **right** side where $n = N_1 + 1 \ldots 2N_1$, $n_r = n - N_1$, $\boldsymbol{d} = \boldsymbol{u}_y$:

$$\boldsymbol{x}_n = \boldsymbol{x}_0^r + \boldsymbol{u}_y \sum_{i=1}^{n_r} \Delta_i \tag{65a}$$

$$V_n = (\boldsymbol{u}_y \cdot \hat{\boldsymbol{E}}_T^{pl})\, \mathrm{e}^{\mathrm{i}\boldsymbol{k}_T^i \cdot \boldsymbol{x}_n} (\mathrm{i}k_y^i)^{-1} \big(\mathcal{T}(-k_y^i \Delta_{n_r}) - \mathcal{T}(k_y^i \Delta_{n_r+1})\big) \tag{65b}$$

$$\boldsymbol{J}_n(\boldsymbol{r}_T) = \mathcal{J}(\boldsymbol{x}; \boldsymbol{x}_n, \boldsymbol{u}_y, \Delta_{n_r}, \Delta_{n_r+1}, w), \tag{65c}$$

$$\boldsymbol{K}_n(\boldsymbol{r}_T) = \mathcal{K}(\boldsymbol{x}; \boldsymbol{x}_n, \boldsymbol{u}_y, \Delta_{n_r}, \Delta_{n_r+1}), \tag{65d}$$

the **upper** side where $n = 2N_1 + 1 \ldots 3N_1$, $n_u = n - 2N_1$, $\boldsymbol{d} = \boldsymbol{u}_x$:

$$\boldsymbol{x}_n = \boldsymbol{x}_0^u + \boldsymbol{u}_x \sum_{i=1}^{n_u} \Delta_i \tag{66a}$$

$$V_n = (\boldsymbol{u}_x \cdot \hat{\boldsymbol{E}}_T^{pl})\, \mathrm{e}^{\mathrm{i}\boldsymbol{k}_T^i \cdot \boldsymbol{x}_n} (\mathrm{i}k_x^i)^{-1} \big(\mathcal{T}(-k_x^i \Delta_{n_u}) - \mathcal{T}(k_x^i \Delta_{n_u+1})\big) \tag{66b}$$

$$\boldsymbol{J}_n(\boldsymbol{r}_T) = \mathcal{J}(\boldsymbol{x}; \boldsymbol{x}_n, \boldsymbol{u}_x, \Delta_{n_u}, \Delta_{n_u+1}, w), \tag{66c}$$

$$\boldsymbol{K}_n(\boldsymbol{r}_T) = \mathcal{K}(\boldsymbol{x}; \boldsymbol{x}_n, \boldsymbol{u}_x, \Delta_{n_u}, \Delta_{n_u+1}), \tag{66d}$$

the **left** side where $n = 3N_1 + 1 \ldots 4N_1 = N$, $n_l = n - 3N_1$, $\boldsymbol{d} = \boldsymbol{u}_y$:

$$\boldsymbol{x}_n = \boldsymbol{x}_0^l + \boldsymbol{u}_y \sum_{i=1}^{n_l} \Delta_i \tag{67a}$$

$$V_n = (\boldsymbol{u}_y \cdot \hat{\boldsymbol{E}}_T^{pl})\, \mathrm{e}^{\mathrm{i}\boldsymbol{k}_T^i \cdot \boldsymbol{x}_n} (\mathrm{i}k_y^i)^{-1} \big(\mathcal{T}(-k_y^i \Delta_{n_l}) - \mathcal{T}(k_y^i \Delta_{n_l+1})\big) \tag{67b}$$

$$\boldsymbol{J}_n(\boldsymbol{r}_T) = \mathcal{J}(\boldsymbol{x}; \boldsymbol{x}_n, \boldsymbol{u}_y, \Delta_{n_l}, \Delta_{n_l+1}, w), \tag{67c}$$

$$\boldsymbol{K}_n(\boldsymbol{r}_T) = \mathcal{K}(\boldsymbol{x}; \boldsymbol{x}_n, \boldsymbol{u}_y, \Delta_{n_l}, \Delta_{n_l+1}), \tag{67d}$$

The necessary expressions for $\hat{\alpha}_{nn'}^{(j)}(\boldsymbol{k}, \rho)$ and $\bar{\bar{\alpha}}_{nn'}^{(j)}(\boldsymbol{x}, \rho)$ are given above in the tables of section 7.3.

10 The single homogeneous layer

10.1 Reflection and transmission coefficients

For a single homogeneous layer ($p = 2$) of thickness d, between regions $p = 1$ and $p = 3$, where we have explicitly for $R = R^e, R^h$

$$R^{\cdot} = R_{12}^{\cdot} + \frac{T_{12}^{\cdot} R_{23}^{\cdot} T_{21}^{\cdot} \exp(-2\gamma_2 d)}{1 - R_{21}^{\cdot} R_{23}^{\cdot} \exp(-2\gamma_2 d)}, \tag{68}$$

where

$$R_{pq}^e = \frac{\gamma_q \varepsilon_p - \gamma_p \varepsilon_q}{\gamma_q \varepsilon_p + \gamma_p \varepsilon_q}, \qquad T_{pq}^e = \frac{2\gamma_p \varepsilon_q}{\gamma_q \varepsilon_p + \gamma_p \varepsilon_q}, \tag{69}$$

$$R_{pq}^h = \frac{\gamma_q \mu_p - \gamma_p \mu_q}{\gamma_q \mu_p + \gamma_p \mu_q}, \qquad T_{pq}^h = \frac{2\gamma_p \mu_q}{\gamma_q \mu_p + \gamma_p \mu_q}. \tag{70}$$

10.2 Asymptotic expansions for large k

Estimates for the constant $c_1^{(j)}, c_2^{(j)}$ can be obtained numerically by (at least) 2 values of g_j, say $q_1 = g_j(k_1)$ and $q_2 = g_j(k_2)$, as follows

$$c_1 = \frac{k_1^3 q_1 - k_2^3 q_2}{k_1^2 - k_2^2}, \qquad c_2 = -k_1^2 k_2^2 \frac{k_1 q_1 - k_2 q_2}{k_1^2 - k_2^2}. \tag{71}$$

More accurate values are possible if we can expand the reflection coefficients analytically, for example for the case of a single homogeneous layer.

To obtain asymptotic expansions of $g_1(k)$ and $g_2(k)$ for large k, we start with the asymptotic expansions of γ_p and R^e and R^h. Define

$$\delta = \frac{\omega^2}{2k^2}, \tag{72}$$

so large k corresponds with small δ. First, we have

$$\gamma_p(k) = k\big(1 - 2\delta\varepsilon_p\mu_p\big)^{\frac{1}{2}} = k\big(1 - \delta\varepsilon_p\mu_p + \ldots\big). \tag{73}$$

It should be noted that this asymptotic expansion is valid for small $\delta\varepsilon_p\mu_p = \delta/c_p^2$, in other words for $k \gg \omega/c_p = k_{\text{free field}}$. When $\omega = 2\pi f$, c is a typical wave speed, and $a \sim 2\pi/b$ is a typical cell size, then m has to be larger than the cell Helmholtz number

$$\boxed{m \gg \frac{fa}{c}.} \tag{74}$$

For example: if $f = 1 \cdot 10^9$ Hz, $c = 3 \cdot 10^8$ m/s, and $a = 0.1$ m, then $m \gg 0.3$. So if these values are sufficiently characteristic of the type of problems to be considered, this asymptotic behaviour seems become apparent almost immediately, which is very fortunate.

This is of course separate from the condition that the neglected terms in the Kummer-reduced summation, which are $O(1/m^8)$ (eq. 26), should be small enough (the first part of expression 23).

We continue with the reflection coefficients

$$R^e = R_{12}^e + \text{EST} \simeq \frac{\gamma_2\varepsilon_1 - \gamma_1\varepsilon_2}{\gamma_2\varepsilon_1 + \gamma_1\varepsilon_2} = \frac{\varepsilon_1 - \varepsilon_2}{\varepsilon_1 + \varepsilon_2}\Big(1 + 2\delta\varepsilon_1\varepsilon_2 \frac{\varepsilon_1\mu_1 - \varepsilon_2\mu_2}{\varepsilon_1^2 - \varepsilon_2^2} + \ldots\Big), \tag{75}$$

$$R^h = R_{12}^h + \text{EST} \simeq \frac{\gamma_2\mu_1 - \gamma_1\mu_2}{\gamma_2\mu_1 + \gamma_1\mu_2} = \frac{\mu_1 - \mu_2}{\mu_1 + \mu_2}\Big(1 + 2\delta\mu_1\mu_2 \frac{\varepsilon_1\mu_1 - \varepsilon_2\mu_2}{\mu_1^2 - \mu_2^2} + \ldots\Big), \tag{76}$$

where it is assumed that the layer thickness d is not very small. Otherwise we have to obey another condition for m, such that $2\gamma_2 d \sim 2kd \sim 2mbd$ is large enough to ignore the exponential terms:

$$\boxed{m \gg \frac{a}{4\pi d}.} \tag{77}$$

With this, we derive

$$\tfrac{1}{2}(R^e - 1) = -\frac{\varepsilon_2}{\varepsilon_1 + \varepsilon_2} + \delta\varepsilon_1\varepsilon_2 \frac{\varepsilon_1\mu_1 - \varepsilon_2\mu_2}{(\varepsilon_1 + \varepsilon_2)^2} + \dots \tag{78}$$

$$\tfrac{1}{2}(R^h + 1) = \frac{\mu_1}{\mu_1 + \mu_2} + \delta\mu_1\mu_2 \frac{\varepsilon_1\mu_1 - \varepsilon_2\mu_2}{(\mu_1 + \mu_2)^2} + \dots \tag{79}$$

$$\gamma_1 \frac{R^e - 1}{2k} = -\frac{\varepsilon_2}{\varepsilon_1 + \varepsilon_2} + \delta\Big(\varepsilon_1\mu_1 \frac{\varepsilon_2}{\varepsilon_1 + \varepsilon_2} + \varepsilon_1\varepsilon_2 \frac{\varepsilon_1\mu_1 - \varepsilon_2\mu_2}{(\varepsilon_1 + \varepsilon_2)^2}\Big) + \dots \tag{80}$$

$$k \frac{R^h + 1}{2\gamma_1} = \frac{\mu_1}{\mu_1 + \mu_2} + \delta\Big(\varepsilon_1\mu_1 \frac{\mu_1}{\mu_1 + \mu_2} + \mu_1\mu_2 \frac{\varepsilon_1\mu_1 - \varepsilon_2\mu_2}{(\mu_1 + \mu_2)^2}\Big) + \dots \tag{81}$$

Noting that $\varepsilon_0 = \varepsilon_1$ and $\mu_0 = \mu_1$, we have finally

$$g_1(k) = \frac{\mathrm{i}}{\omega k \varepsilon_1}\Bigg[\frac{\varepsilon_2}{\varepsilon_1 + \varepsilon_2} + \frac{\omega^2}{2k^2}\Big(\varepsilon_1\mu_1 \frac{2\mu_1}{\mu_1 + \mu_2} - \varepsilon_1\mu_1 \frac{\varepsilon_2}{\varepsilon_1 + \varepsilon_2} - \varepsilon_1\varepsilon_2 \frac{\varepsilon_1\mu_1 - \varepsilon_2\mu_2}{(\varepsilon_1 + \varepsilon_2)^2}\Big) + \dots\Bigg], \tag{82}$$

$$g_2(k) = \frac{\mathrm{i}\omega\mu_1}{k}\Bigg[\frac{\mu_1}{\mu_1 + \mu_2} + \frac{\omega^2}{2k^2}\Big(\varepsilon_1\mu_1 \frac{\mu_1}{\mu_1 + \mu_2} + \mu_1\mu_2 \frac{\varepsilon_1\mu_1 - \varepsilon_2\mu_2}{(\mu_1 + \mu_2)^2}\Big) + \dots\Bigg]. \tag{83}$$

And so the asymptotic coefficients become

$$c_1^{(1)} = \frac{\mathrm{i}\varepsilon_2}{\omega\varepsilon_1(\varepsilon_1 + \varepsilon_2)}, \tag{84}$$

$$c_2^{(1)} = \tfrac{1}{2}\mathrm{i}\omega\Big(\frac{2\mu_1^2}{\mu_1 + \mu_2} - \frac{\varepsilon_2\mu_1}{\varepsilon_1 + \varepsilon_2} - \varepsilon_2 \frac{\varepsilon_1\mu_1 - \varepsilon_2\mu_2}{(\varepsilon_1 + \varepsilon_2)^2}\Big), \tag{85}$$

$$c_1^{(2)} = \frac{\mathrm{i}\omega\mu_1^2}{\mu_1 + \mu_2}, \tag{86}$$

$$c_2^{(2)} = \frac{\frac{1}{2}\mathrm{i}\omega^3\mu_1^2}{\mu_1 + \mu_2}\Big(\varepsilon_1\mu_1 + \mu_2 \frac{\varepsilon_1\mu_1 - \varepsilon_2\mu_2}{\mu_1 + \mu_2}\Big). \tag{87}$$

11 Examples

An example of a gridded square (figure 8) is evaluated for the following parameter values (TE-excitation):

$[\mathcal{R}_P]_{\mathrm{dB}}$	= −4.41 dB	a_2	= 8.4 mm
c_0	= $3 \cdot 10^8$ meter/sec ,	L_1	= 6.7 mm,
μ_0	= $1.2566371 \cdot 10^{-6}$ henry/meter ,	L_2	= 8.4 mm,
ε_0	= $8.8541853 \cdot 10^{-12}$ farad/meter ,	w_1	= 1.0 mm,
ω	= $2\pi \cdot 10 \cdot 10^9$ Hz ,	w_2	= 1.0 mm,
λ_0	= 29.97925 mm ,	x_c	= 3.7 mm,
k_0	= 209.58447 /meter ,	y_c	= 4.7 mm,
ε	= [1, 3.5, 1] ε_0 farad/meter ,	N_1	= 6 ,
μ	= [1, 1, 1] μ_0 henry/meter ,	N_2	= 8 ,
$\boldsymbol{u}^i$	= [0.59482639, 0,0.8038542] ,	$M_{1,\mathrm{re}}$	= 30 ,
φ^i	= 0.0 rad ,	$M_{2,\mathrm{re}}$	= 30 ,
θ^i	= 0.63704966 rad ,	$M_{1,\mathrm{lo}}$	= 2 ,
$\boldsymbol{k}^i$	= [124.66638, 0, 168.47536] ,	$M_{2,\mathrm{lo}}$	= 2 ,

$\boldsymbol{u}^p$ = [0.8038542, 0,-0.59482639] , $M_{1,\mathrm{hi}} = 2$,
$\varphi^p = -\frac{1}{2}\pi$ rad , $M_{2,\mathrm{hi}} = 2$,
$\theta^p = \frac{1}{2}\pi$ rad , $\lambda_\rho = 4$,
$E^i = 10^6 \exp(\frac{3}{4}\pi \mathrm{i})$, $\rho_{\max} = 0.4$,
$d = 70\ \mu$m , $\rho_1 = 0.2$,
$a_1 = 8.4$ mm , $[\rho] = 81$.

In the case of TM excitation we have instead $\theta^p = \frac{1}{2}\pi + \theta^i$ and $\phi^p = 0$, leading to $[\mathcal{R}_P]_{\mathrm{dB}} = -7.14$ dB.

The parameters denote the following.

- $[\mathcal{R}_P]_{\mathrm{dB}} = 10\,^{10}\log(\mathcal{R}_P)$ denotes the power reflection coefficient (21) in decibels.
- $c_0 = (\mu_0\varepsilon_0)^{-1/2}$ is the free field light speed.
- μ_0 and μ are the permeabilities of free field, and of the upper medium, the layer, and the lower medium.
- ε_0 and ε are the permittivities of free field, and of the upper medium, the layer, and the lower medium.
- ω is the circular frequency.
- λ_0 is free field wave length.
- $k_0 = \omega/c_0$ is free field wave number.
- $\boldsymbol{u}^i$ is the propagation direction of incident wave.
- φ^i is the angle of $\boldsymbol{u}^i$ in the (x, y)-plane.
- θ^i is the angle of $\boldsymbol{u}^i$ with the z-axis.
- $\boldsymbol{k}^i = \boldsymbol{u}^i\omega/c_0$ is the incident wave vector.
- $\boldsymbol{u}^p$ is the direction of E-polarization of incident wave.
- φ^p the angle of $\boldsymbol{u}_p$ in the (x, y)-plane.
- θ^p the angle of $\boldsymbol{u}_p$ with the z-axis.
- E^i complex amplitude of incident wave $\boldsymbol{E}^i$.
- d is the thickness of the layer.
- a_1 and a_2 are length of vectors $\boldsymbol{a}_1 = a_1\boldsymbol{u}_x$ and $\boldsymbol{a}_2 = a_2\boldsymbol{u}_y$.
- L_1 and L_2 are the lengths of the squares, measured outside.
- w_1 and w_2 are the widths of the sides of the squares.
- $(x_c, y_c$ are the coordinates of the centre of the squares.
- N_1 and N_2 are the number of basis functions at an edge of the inner (1) and outer (2) square (note that the outer square is part of a grid, and therefore only 2 sides of the outer square are included in a cell).
- $|m_1| \le M_{1,\mathrm{re}}$ and $|m_2| \le M_{2,\mathrm{re}}$ are the ranges used for the calculation of the reduced double series for $Z^{(j)}_{nn'}$ in equation 23 (the same for both $j = 1$, $j = 2$).
- $|m_1| \le M_{1,\mathrm{lo}}$ and $|m_2| \le M_{2,\mathrm{lo}}$, respectively $|m_1| \le M_{1,\mathrm{hi}}$ and $|m_2| \le M_{2,\mathrm{hi}}$ are the ranges used for the evaluation of the double series in the lower, respectively higher ρ-integral for $\zeta^{(j)}_{nn'}$ of equation (40).
- λ_ρ denotes the auxiliary λ parameter in the ρ transformation for $\zeta^{(j)}_{nn'}$.
- $\rho_{\max}$ denotes the upper limit of integration (approximating "$\rho = \infty$") in the ρ-integral for $\zeta^{(j)}_{nn'}$ (equation 40).

- ρ_1 denotes the transition point between the "low" and the "high" ρ-integration (equation 40).
- $[\rho]$ denotes the size of the discretized ρ-vector (including $\rho = 0$) used for the numerical integration of the ρ-integration (equation 40). Note that this should be odd because the Simpson integration algorithm is used.

We have plotted in figure (9) representative parts of the ρ-integrands of $\zeta_{nn'}^{(j)}$. Specifically, we have along $(0, \rho_1]$

$$\det(\boldsymbol{A}) \sum_{m_1=-\infty}^{\infty} \sum_{m_2=-\infty}^{\infty} \mathrm{e}^{-\mathrm{i}\boldsymbol{A}\boldsymbol{m}\cdot\boldsymbol{k}_T^i} \bar{\bar{\alpha}}_{nn'}^{(j)}(\boldsymbol{A}\boldsymbol{m}, \rho)$$

and along $[\rho_1, \infty)$

$$\sum_{m_1=-\infty}^{\infty} \sum_{m_2=-\infty}^{\infty} \hat{\epsilon}(\boldsymbol{B}\boldsymbol{m} + \boldsymbol{k}_T^i, \rho)\hat{\alpha}_{nn'}^{(j)}(\boldsymbol{B}\boldsymbol{m} + \boldsymbol{k}_T^i).$$

This is to confirm that the rather small m-summation ($M_{1,\mathrm{lo}} = M_{2,\mathrm{lo}} = M_{1,\mathrm{hi}} = M_{2,\mathrm{hi}} = 2$) used to construct these integrands is large enough, and that the transition point ρ_1 is well chosen: the discontinuity at the connection in ρ_1 is indeed negligible. In fact, a summation over only 3 terms (*i.e.* $M_{1,\mathrm{lo}} = \ldots = 1$) would have been sufficient as well. Furthermore, the upperlimit $\rho_{\max} = 0.4$ is also high enough for the integrands to be vanishingly small.

The number of terms of the reduced m-summation ($M_{1,\mathrm{re}} = M_{2,\mathrm{re}} = 30$) is rather high. This is because of the relatively thin layer (small d). However, as long as we can reach the M values for which the acceleration process becomes valid, this is of no real concern since this reduced summation is relatively cheap.

This number of terms is chosen as follows, obeying the two conditions on m given in equations (74) and (77).

(i) On the one hand, m should be larger than the cell Helmholtz number, which is here $\omega a_1/2\pi c_0 = 0.28$. So any $M \geq 1$ would be sufficient to satisfy this.

(ii) On the other hand, however, the thickness d of the layer is just too small to make the exponential $\mathrm{e}^{-2\gamma_2 d}$ already vanishingly small for low values of m. So we have to consider the condition given in equation (77) and increase $M_{1,\mathrm{re}}$ and $M_{2,\mathrm{re}}$ until $m \gg a_1/4\pi d = 9.5$. It appeared that with $m > 30$, $\mathrm{e}^{-2\gamma_2 d} < 0.011$ and sufficiently small.

(iii) The order of magnitude of the neglected terms in the reduced summation, $O(1/m^6)$, should be small enough. For $m = 30$ this is $1.4{\cdot}10^{-9}$ which is indeed very small.

The figures (10, 14, 12, 16) present the physical results in the form of the axial current density. They are compared with similar results (11, 13, 15, 17), provided by B. Morsink, Thales Naval Nederland, and produced independently from us by a Finite Element method. The Thales results are of particular interest because the corresponding radiation field is favourably compared with experiments.

Both the total field intensities and the more detailed real and imaginary parts of the inner square compare very well. The outer square, however, show a rather more different behaviour. Further investigations are necessary to make sure that the differences are just due to the methods applied.

The figures (19, 18, 21, 20) are similar examples for a strip and a single square. The conditions are practically the same as for the gridded square ($\frac{1}{4}\pi = 0.785$ for the strip), except for the layer thickness d, which is here 7 mm, in order to allow the reduced m-summation limits $M_{\text{re}} = 3$ to be really small. The strip is analysed with both a single density grid (like figure 6 with $N_{\text{side}} = 10$) and with a double density grid (figure 8 with $N_{\text{side}} = 20$). The difference (for this frequency) in the axial current component and in the reflection coefficient is negligible. Note that the transversal current component is important near the strip ends.

In figure (22) the reflection coefficients (in dB) for the above cases (TE-polarization) are plot as functions of frequency between 1 GHz and 31 GHz. The frequency selective surface is clearly almost transparent around 12 GHz. It may be observed that especially for higher frequencies the numerical accuracy of the used grid is not high enough, as the calculations become unstable with the reflection coefficient sometimes exceeding 1, which is physically impossible. The on-set of this numerical instability is especially clear in the case of the strip, where both the results for the single and double density grid is plot. It appears that the wiggles for lower frequencies are not to be attributed to numerical inaccuracy, at least for the strip. For the other geometries the important corner areas are poorly represented by the present simple basis function distribution, possibly leading to relatively large errors for conditions of total reflection.

12 Conclusions

A general theory is presented to accelerate slowly converging series, that occur in the numerical solution of the electromagnetic scattering problem of Frequency Selective Surfaces. It consists of three steps. (1) A Kummer transformation-type step, where the asymptotically slow part ($O(1/k)$, $O(1/k^3)$, etc.) of the Green's function in the series is subtracted, and taken apart. (2) An Ewald transformation-type step, where the algebraically slow converging parts $O(1/k^n)$ are turned into exponentially convergent integrals of the type $\sim \mathrm{e}^{-k^2\rho^2}$. (3) A Poisson transformation step, in order to transform the relatively slow convergence $\sim \mathrm{e}^{-k^2\rho^2}$ for small ρ into a fast convergence $\sim \mathrm{e}^{-k^2/\rho^2}$.

Several conditions for the validity of the method are explicitly given.

Implementation

The technique presented is very general. Therefore, the necessary Fourier transforms are in general not explicitly available and probably have to be evaluated numerically. There is, however, an important class of basis/test functions that do allow an explicit evaluation. These are the so-called *rooftop basis functions*. Especially for a rectangular grid the formulas may be evaluated analytically completely.

We have implemented the method for a strip, a double strip (both "L" and "="), a single square and a gridded square. This last case is compared in some detail with FEM results by B. Morsink (Thales Naval Nederland). The results are very promising.

Further comparison with far field results are planned.

Brief summary of the method

Given the series (in the notation of above)

$$S = \sum_{m_1=-\infty}^{\infty} \sum_{m_2=-\infty}^{\infty} g(k)\hat{\alpha}(\boldsymbol{k}), \quad \text{where } \boldsymbol{k} = \boldsymbol{k}^i + \boldsymbol{B}\boldsymbol{m}, k = |\boldsymbol{k}|, \tag{88}$$

where

$$g(k) = \frac{c_1}{k} + \frac{c_2}{k^2} + \frac{c_3}{k^3} \ldots \quad (k \to \infty). \tag{89}$$

Kummer's transformation yields an improved convergence of the reduced series

$$S = \sum \left\{ \left(g(k) - \frac{c_1}{k} - \frac{c_2}{k^2} - \frac{c_3}{k^3} - \ldots \right) \hat{\alpha}(\boldsymbol{k}) \right\} + c_1 \sum \frac{\hat{\alpha}(\boldsymbol{k})}{k} + c_2 \sum \frac{\hat{\alpha}(\boldsymbol{k})}{k^2} + c_3 \sum \frac{\hat{\alpha}(\boldsymbol{k})}{k^3} + \ldots \tag{90}$$

Slow convergence of the rest is turned into exponential convergence by the couple of transforms:

$$\sum \frac{\hat{\alpha}(\boldsymbol{k})}{k^N} = \frac{2\lambda}{k^N} \int_0^{\infty} \rho^{\lambda N - 1} \sum \hat{\epsilon}(\boldsymbol{k}, \rho)\hat{\alpha}(\boldsymbol{k}) \, \mathrm{d}\rho = \frac{2\lambda}{k^N} \left\{ \det(\boldsymbol{A}) \int_0^{\rho_1} \rho^{\lambda N - 1} \sum \mathrm{e}^{-\mathrm{i}\boldsymbol{A}\boldsymbol{m} \cdot \boldsymbol{k}^i} \bar{\bar{\alpha}}(\boldsymbol{A}\boldsymbol{m}, \rho) \, \mathrm{d}\rho + \int_{\rho_1}^{\infty} \rho^{\lambda N - 1} \sum \hat{\epsilon}(\boldsymbol{k}, \rho)\hat{\alpha}(\boldsymbol{k}) \, \mathrm{d}\rho \right\} \tag{91}$$

Acknowledgements

The contributions of the following colleagues are gratefully acknowledged: J. Boersma, N.G. de Bruijn, U. Das, J.K.M. Jansen, J. Molenaar, B.J. Morsink, W.H.A. Schilders, J. Schipper, A.G. Tijhuis, A.A.F. van de Ven.

References

[1] A.G. TIJHUIS, Plane-Wave Excitation of Two-Dimensionally Periodic Metallized Structures in Plane-Stratified Dielectric Media, January 2002, TUE Report of Study Contract for Thales Naval Nederland B.V.

[2] B.J. MORSINK, S.W. RIENSTRA and A.G. TIJHUIS, Modeling Frequency Selective Surfaces With Multiple Metallization And Continuously Layered Dielectric Substrates, 24th ESTEC Antenna Workshop on Innovative Periodic Antennas: Photonic Bandgap, Fractal and Frequency Selective Structures, ESTEC, 30/5-1/6/2001, Noordwijk, The Netherlands.

[3] A.B. SMOLDERS, *Microstrip Phased-Array Antennas: a Finite Array Approach*, 1994, Thesis Eindhoven University of Technology.

[4] B. DUNNEBIER, Large Microstrip Phased Array Antennas – Analysis and Numerical Implementation, 1999, Final report of the postgraduate program: Information and Communication Technology, Eindhoven University of Technology.

[5] *Computer Techniques for Electromagnetics*, editor: R. Mittra. 1973/1987, Hemisphere / Harper & Row / Springer-Verlag

[6] M. ABRAMOWITZ, and I.A. STEGUN, *Handbook of Mathematical Functions*, National Bureau of Standards, Dover Publications, New York, 1964.

[7] R.P. KANWAL, *Generalized Functions*, 2nd edn., Birkhäuser, Boston, 1998.

[8] S.K. LUCAS, R. SIPCIC, and H.A. STONE, An Integral Equation Solution for the Steady-State Current at a Periodic Array of Surface Microelectrodes, SIAM J. Appl. Math., 1997, **57**(6) p.1615–1638.

[9] R.C. MCCANN, R.D. HAZLETT, and D.K. BABU, Highly accurate approximations of Green's and Neumann functions on rectangular domains, Proceedings of the Royal Society of London **A**, 2001, **457**, p.767–772.

[10] A. DIENSTFREY, F. HANG, and J. HUANG, Lattice Sums and the Two-dimensional, Periodic Green's Function for the Helmholtz equation, Proceedings of the Royal Society of London **A**, 2001, **457**, p.67–85.

[11] S. SINGH, W.F. RICHARDS, J.R. ZINECKER, and D.R. WILTON, Accelerating the Convergence of Series Representing the Free Space Periodic Green's Function, IEEE Transactions on Antennas and Propagation, **38**(12), 1990, p. 1958–1962.

[12] M. PORTO, Ewald summation of electrostatic interactions of systems with finite extent in two of three dimensions, J. Physics A. Math. Gen. **33**, 2000, p. 6211–6218.

[13] R. MITTRA, C.H. CHAN, and T. CWIK, Techniques for Analyzing Frequency Selective Surfaces - A Review, Proceedings of the IEEE, **76**(12), 1988, p.1593–1615.

[14] C.M. LINTON, The Green's Function for the two-dimensional Helmholtz equation in periodic domains, Journal of Engineering Mathematics, **33**(4), 1998, p.377–401.

[15] P. EWALD, Ann. Phys., Lpz. 1921, **64**, p.253

[16] N. GUÉRIN, S. ENOCH, and G. TAYEB, Combined Method for the Computation of Doubly Periodic Green's Function, J. of Electromagn. Waves and Appl., **15**(2), 2001, p.205–221.

13 Figures of Examples

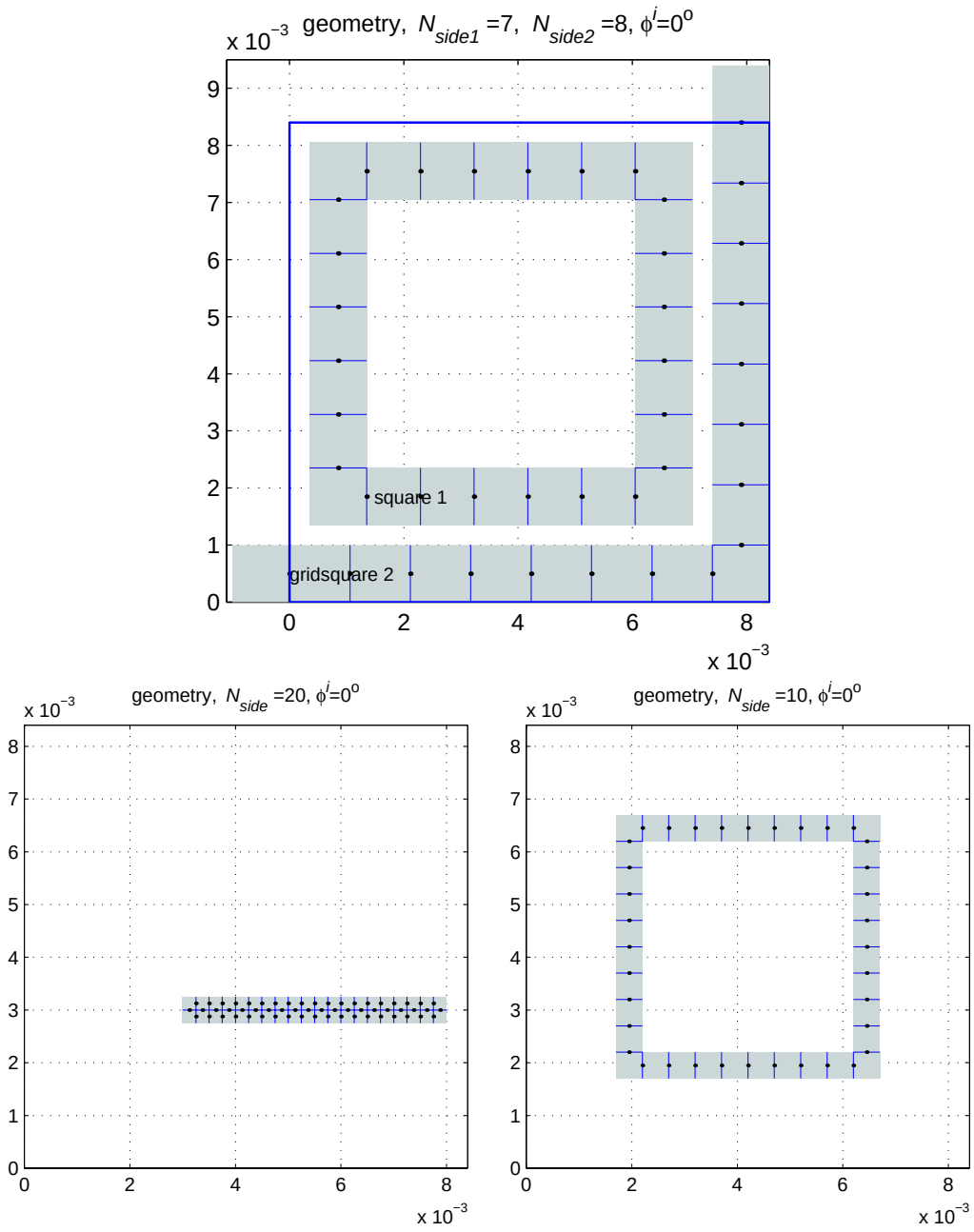

Figure 8: Geometries used for example calculations.

(This page is intentionally left blank.)

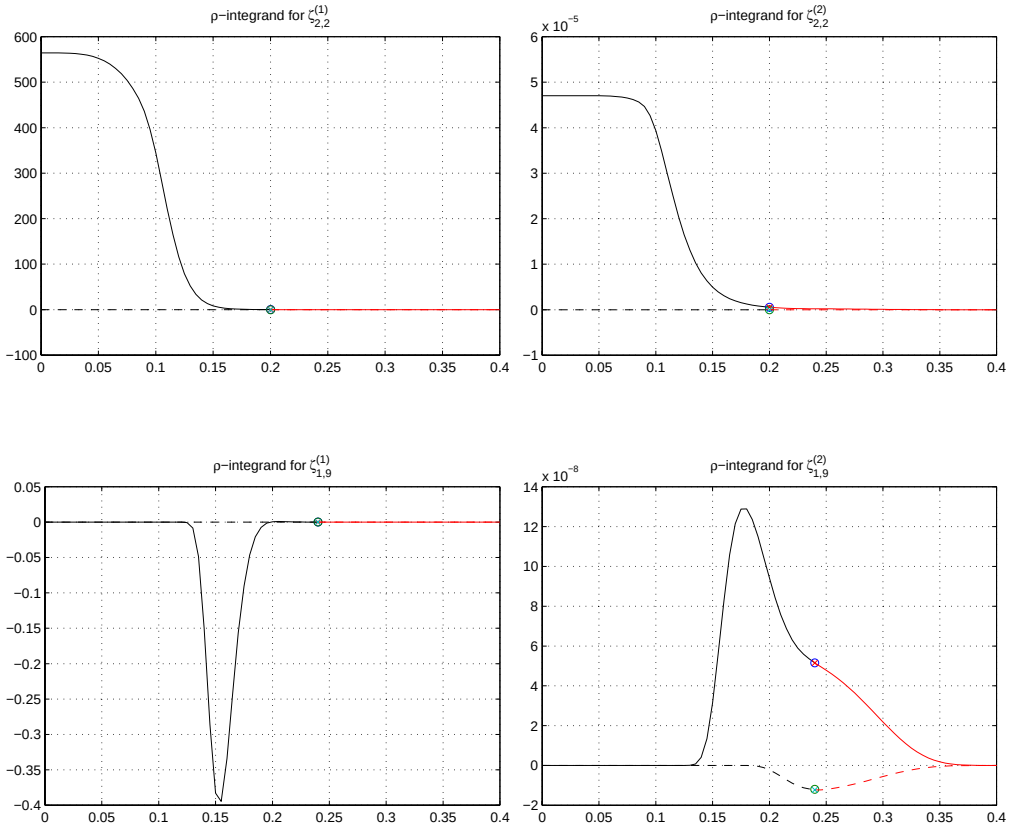

Figure 9: Examples of double-sums in the $\zeta^{(1)}_{nn'}$ and $\zeta^{(2)}_{nn'}$ ρ-integrand for the reduced/low-ρ/large-ρ summmations. Note the jump at ρ_1: $M_{1,\mathrm{lo}}$, $M_{2,\mathrm{lo}}$, $M_{1,\mathrm{hi}}$, and $M_{2,\mathrm{hi}}$ should be large enough such that the jump is negligible.

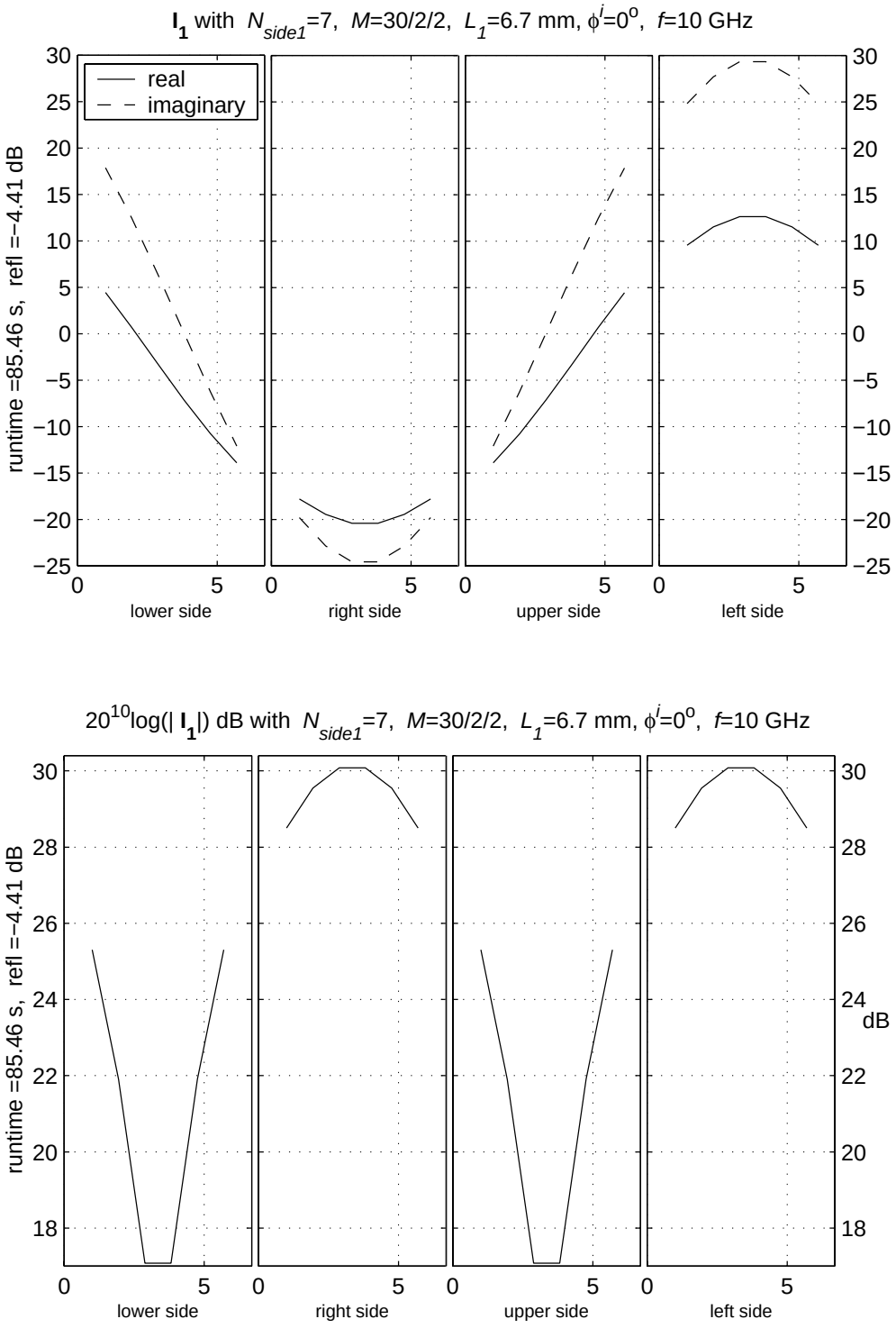

Figure 10: Gridded square, TE inner square. $[\mathcal{R}_P]_{\mathrm{dB}} = -4.41$ dB.

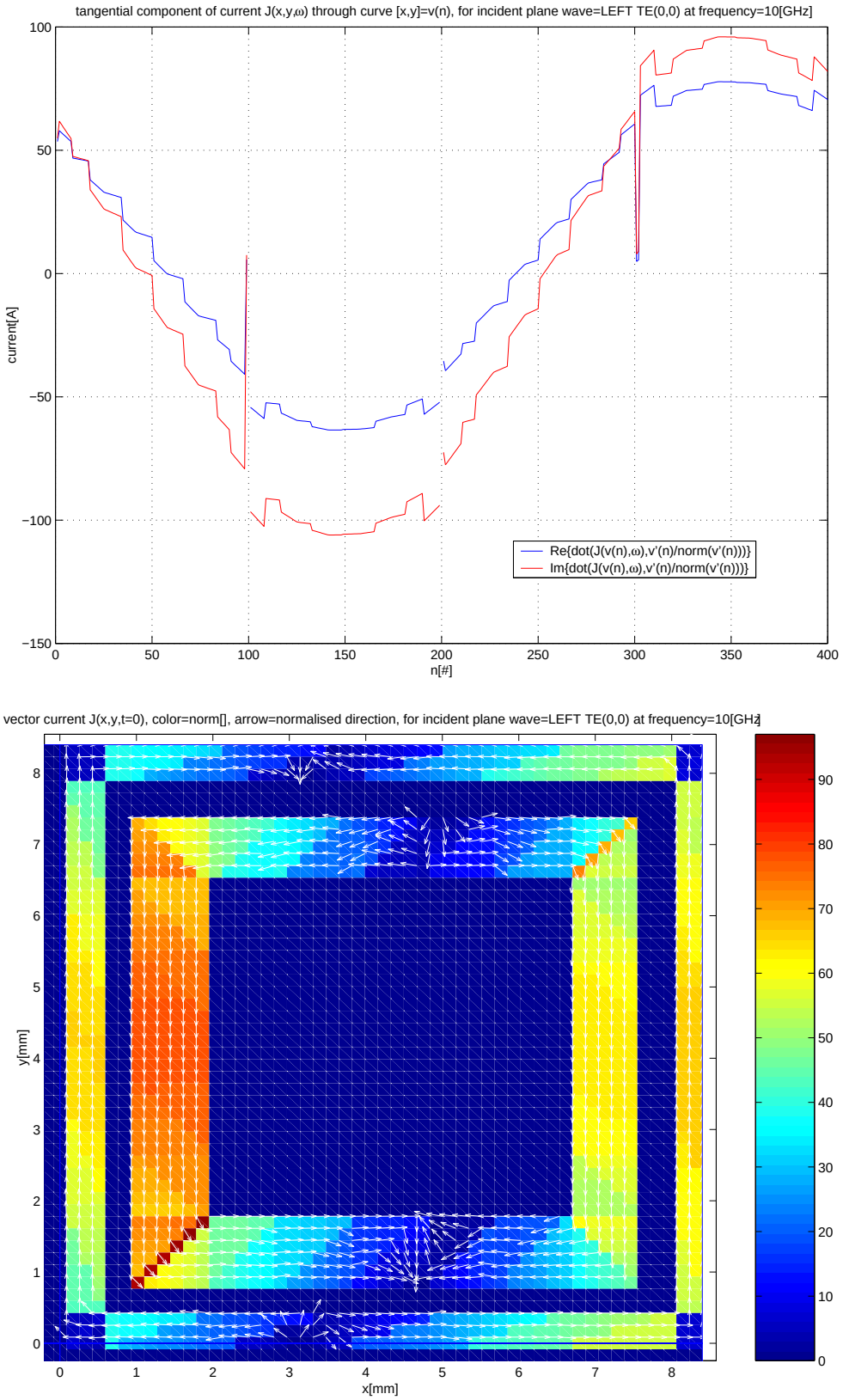

Figure 11: Gridded square, TE inner square. Morsink's result.

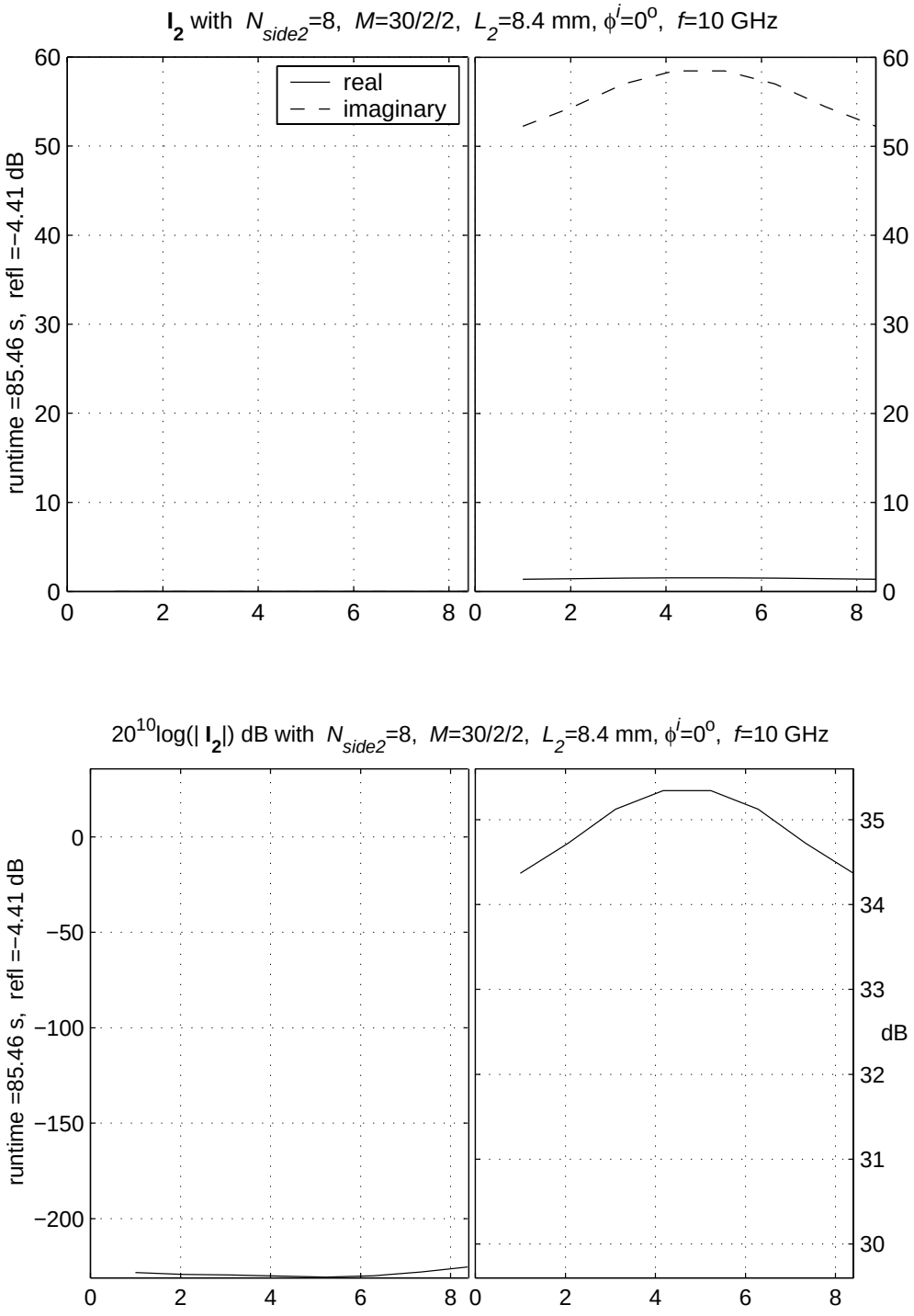

Figure 12: Gridded square, TE outer square. $[\mathcal{R}_P]_{\mathrm{dB}} = -4.41$ dB.

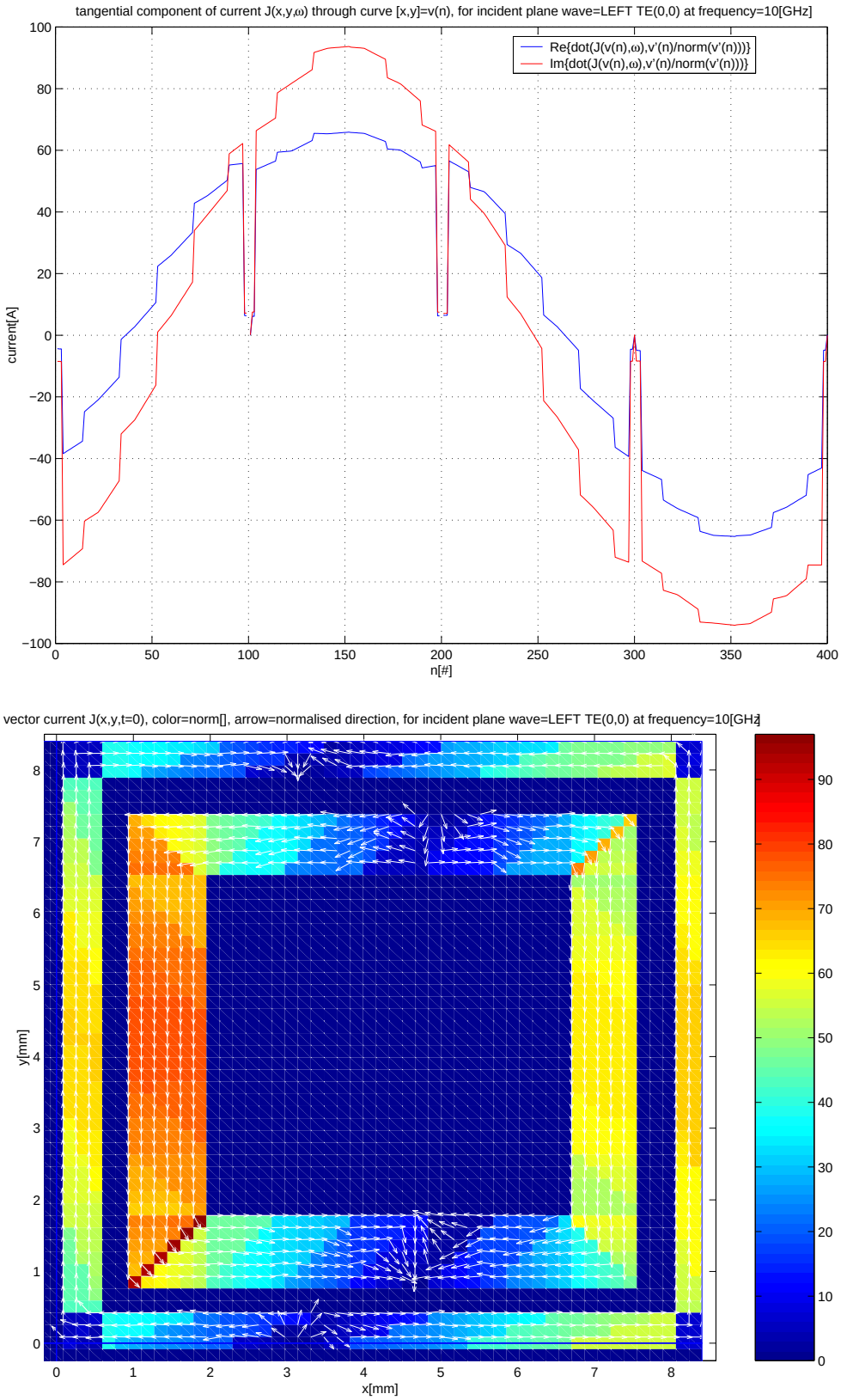

Figure 13: Gridded square, TE outer square. Morsink's result.

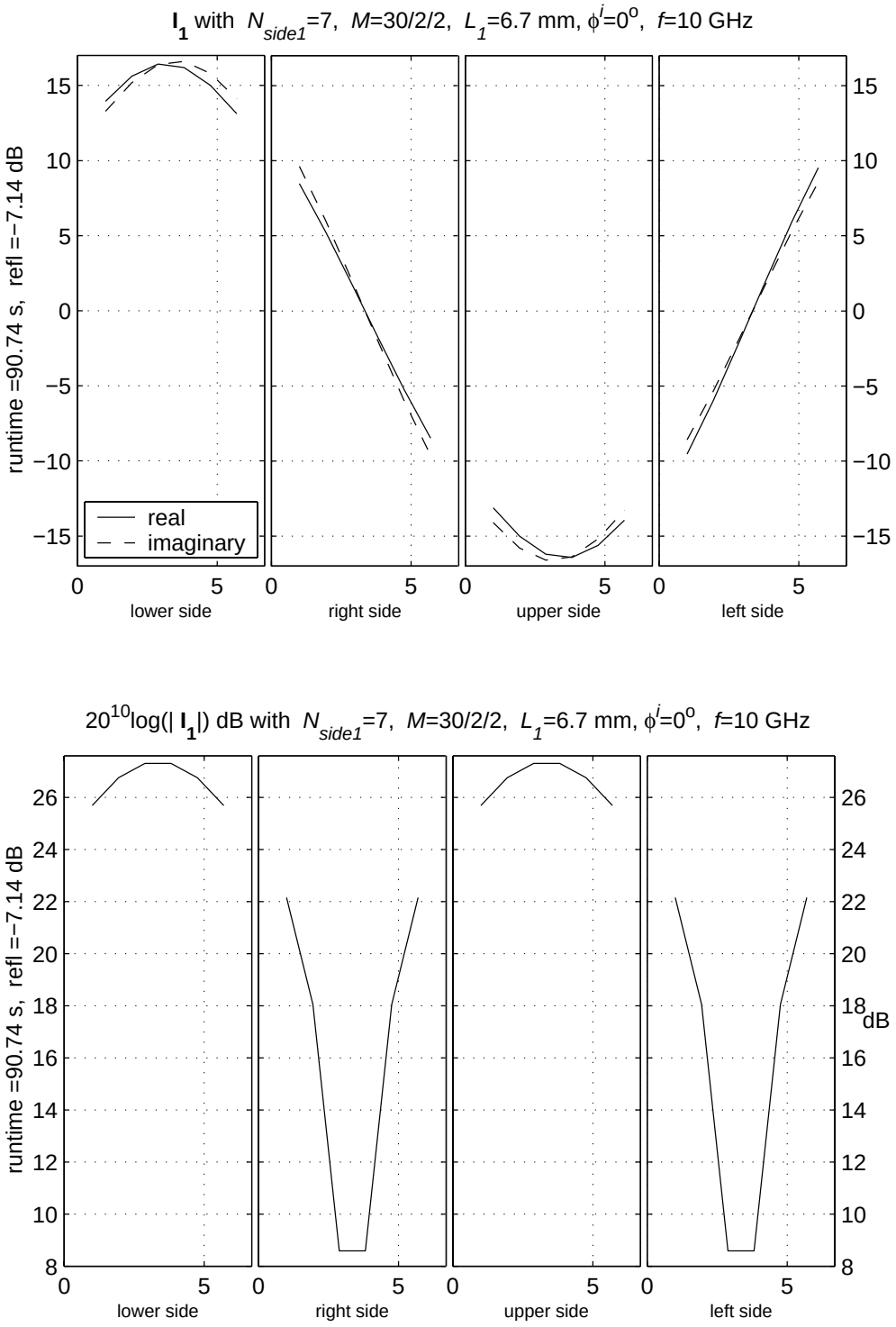

Figure 14: Gridded square, TM inner square. $[\mathcal{R}_P]_{\mathrm{dB}} = -7.14$ dB.

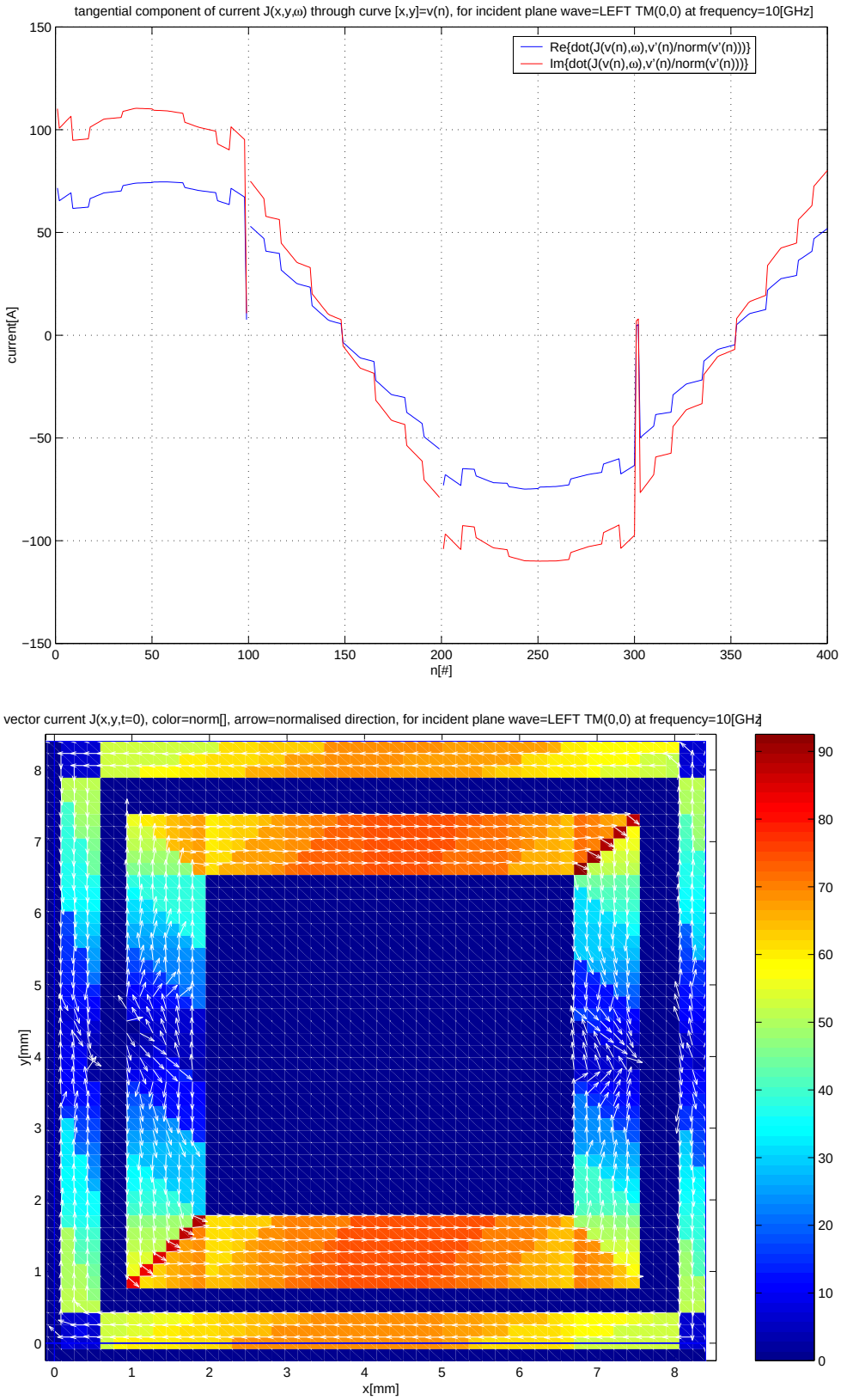

Figure 15: Gridded square, TM inner square. Morsink's result.

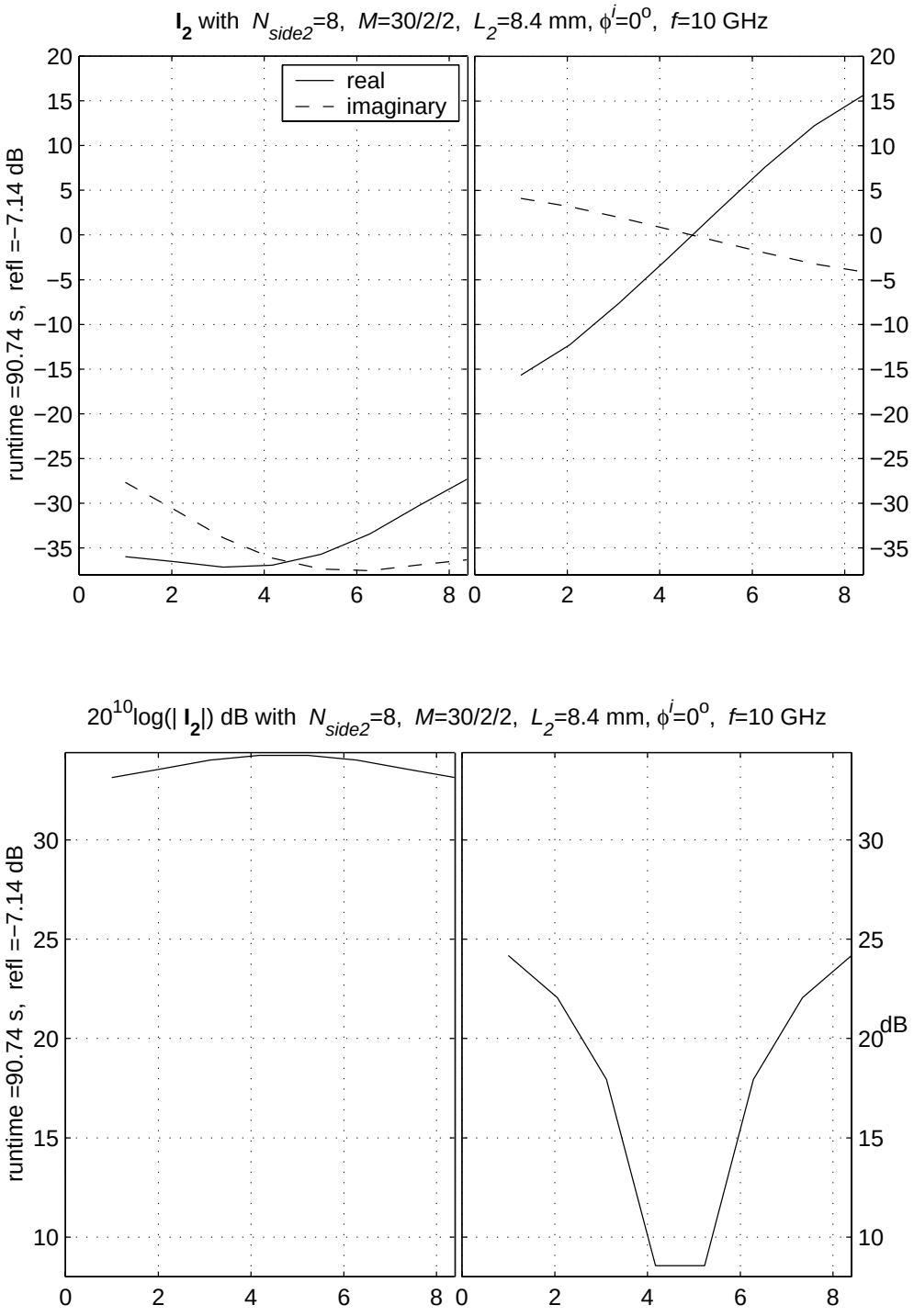

Figure 16: Gridded square, TM outer square. $[\mathcal{R}_P]_{\rm dB} = -7.14$ dB.

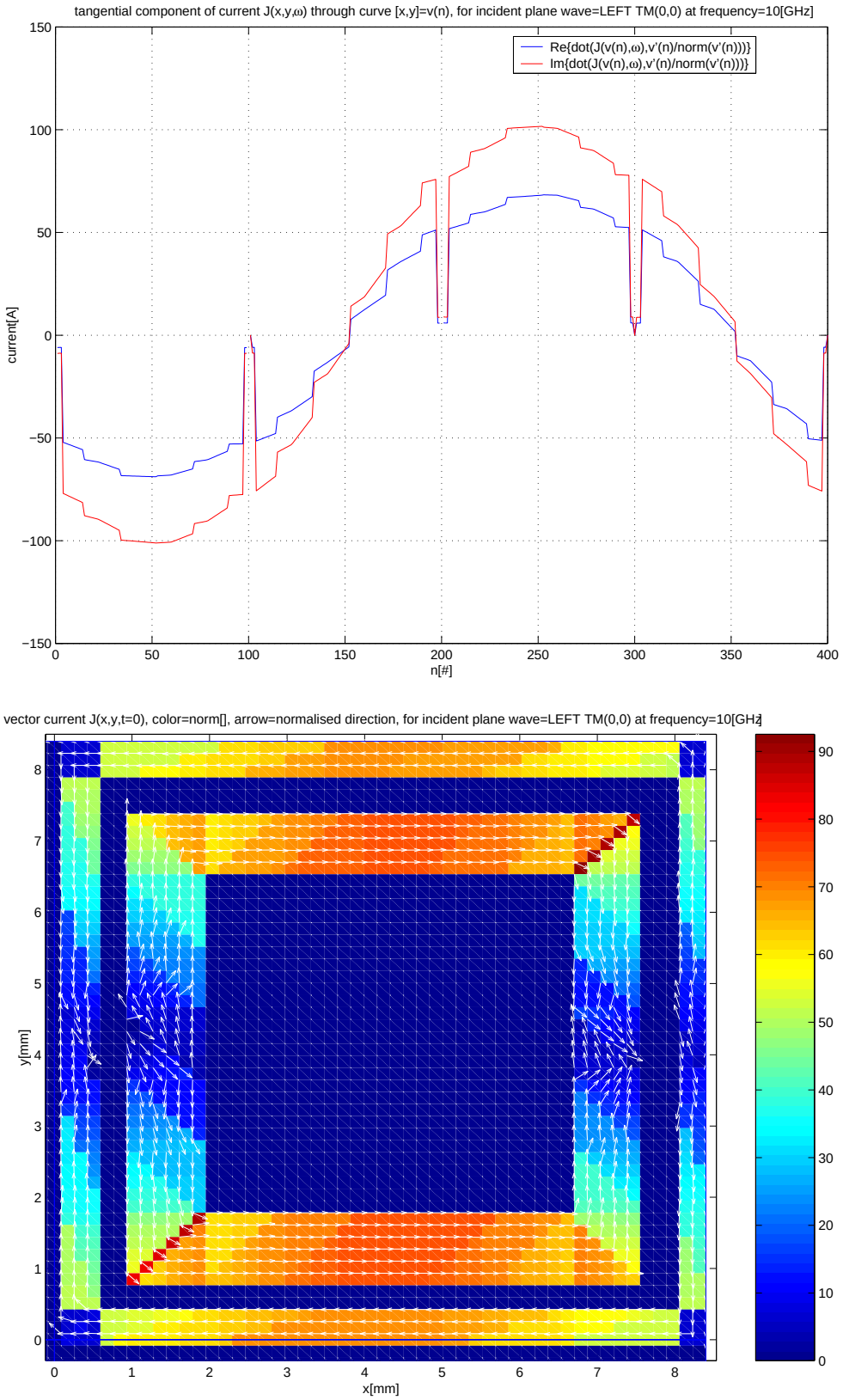

Figure 17: Gridded square, TM outer square. Morsink's result.

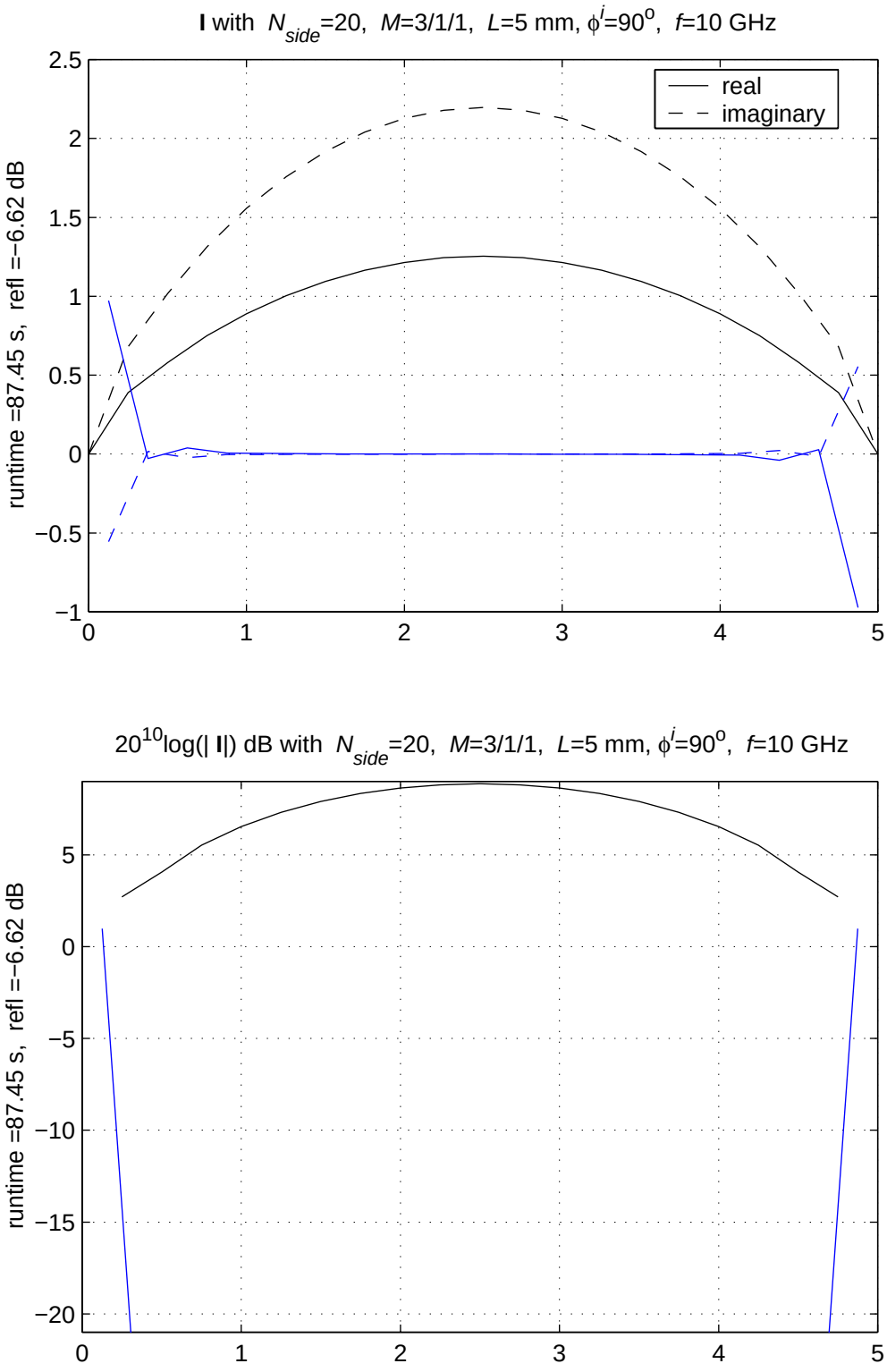

Figure 18: Strip (axial and transversal currents), TE-polarization. $[\mathcal{R}_P]_{\text{dB}} = -6.62$ dB.

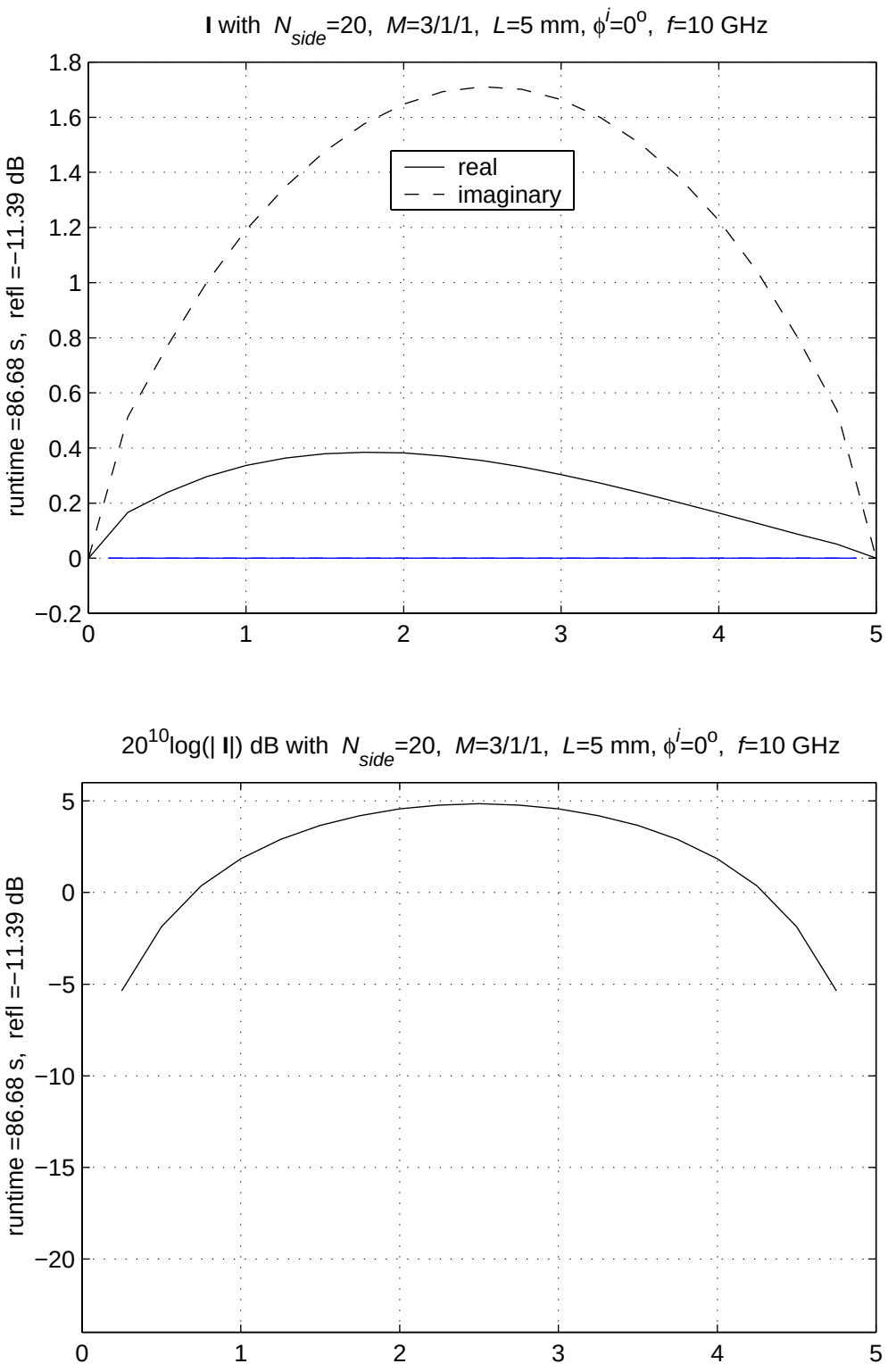

Figure 19: Strip (axial and transversal currents), TM-polarization. $[\mathcal{R}_P]_{\rm dB} = -11.46$ dB.

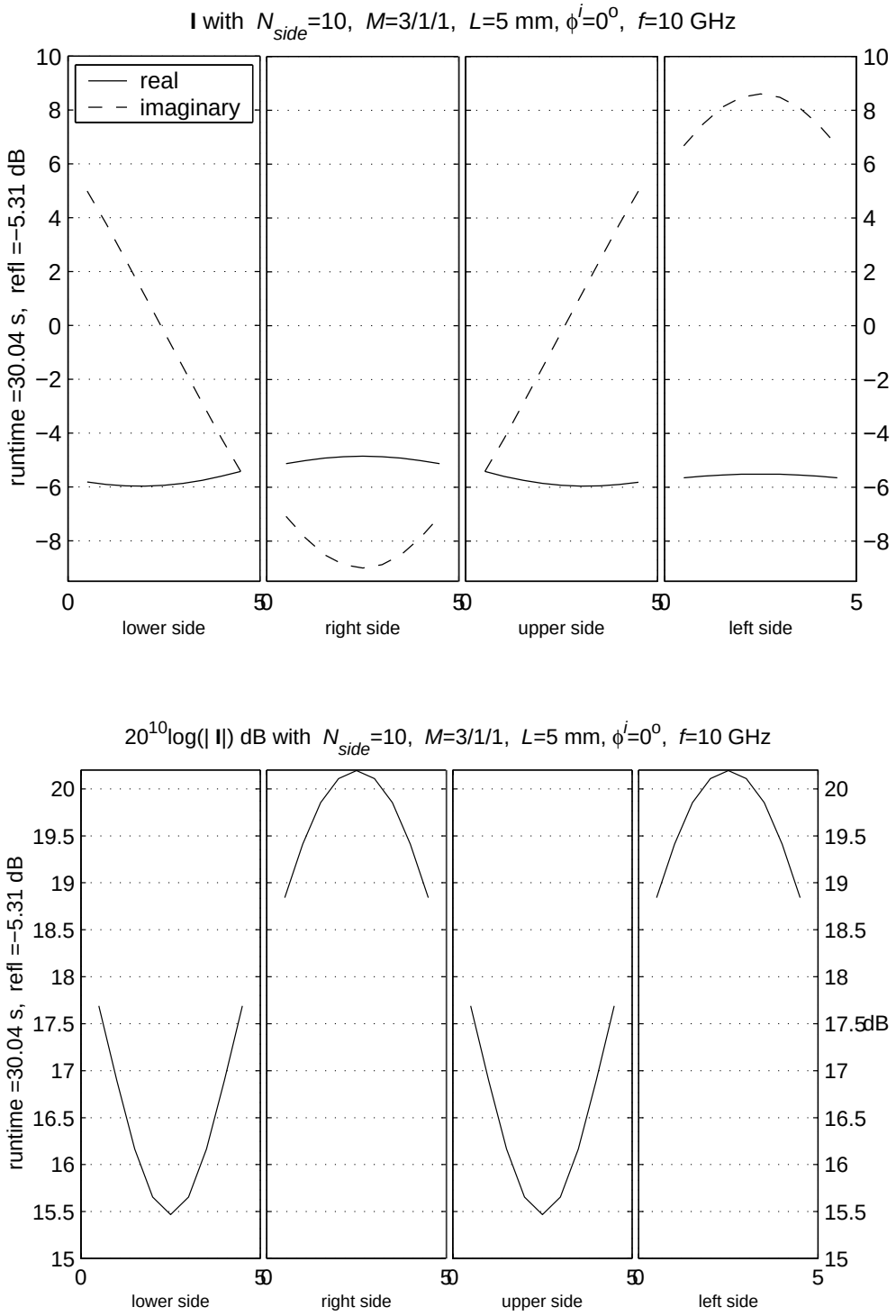

Figure 20: Single square, TE-polarization. $[\mathcal{R}_P]_{\mathrm{dB}} = -5.31$ dB.

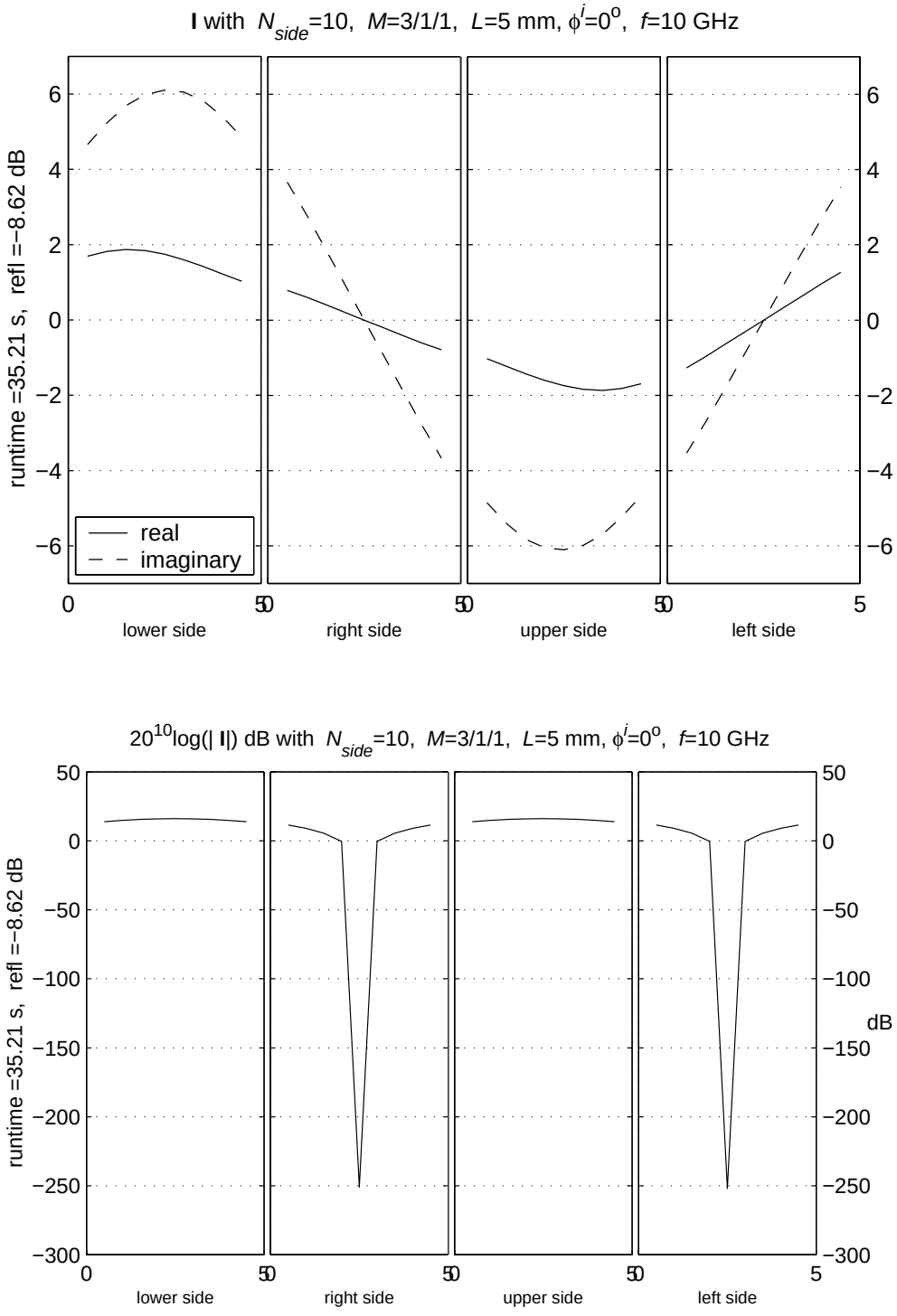

Figure 21: Single square, TM-polarization. $[\mathcal{R}_P]_{\mathrm{dB}} = -8.62$ dB.

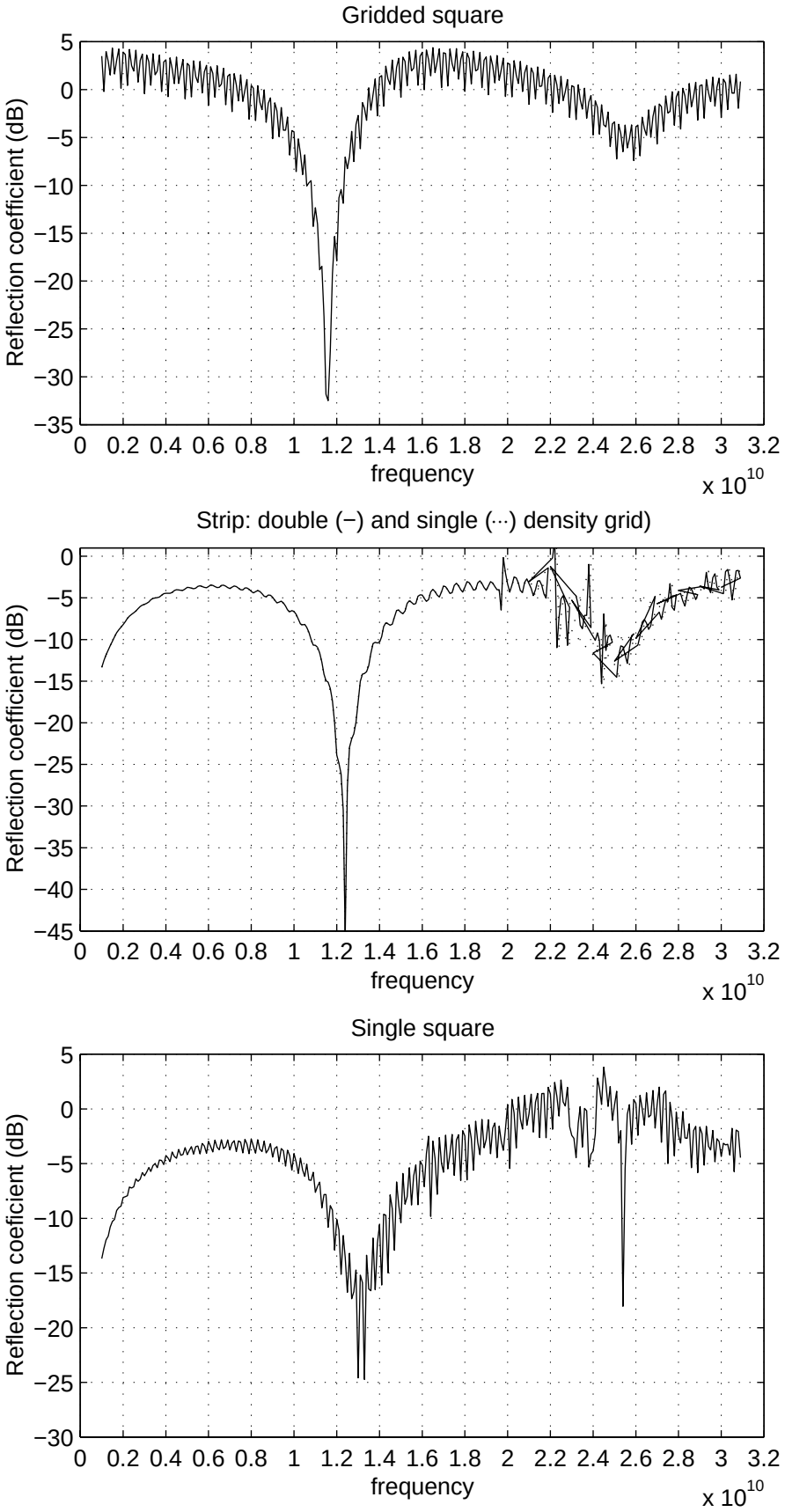

Figure 22: Reflection coefficients (TE) as a function of frequency ($\Delta f = 0.1$ GHz).